Aus dem Lehrstuhl für Experimentelle Ultrahochfeld Magnetresonanz der
Medizinischen Fakultät Charité – Universitätsmedizin Berlin

DISSERTATION

Entwicklung der Multi-Kanal-Hochfrequenz Technologie für Natrium und Kalium Magnet-Resonanz-Tomographie bei 7.0 Tesla: Entwurf und klinische Anwendung

Development of multi-channel radio frequency technology for sodium and potassium magnetic resonance imaging at 7.0 Tesla: design and clinical application

zur Erlangung des akademischen Grades

Dr. rer. medic.

vorgelegt der Medizinischen Fakultät

Charité – Universitätsmedizin Berlin

von

Daniel Wenz

aus Tarnów, Polen

Datum der Promotion: 18.09.2020

Table of Contents

List of Figures 4
Synposis 9
Abstract 9
Abstrakt 11
Introduction 13
Methodology 17
Numerical Electromagnetic Field and Specific Absorption Rate Simulations 17
Benchtop Evaluation 17
Magnetic Resonance Imaging Hardware 18
Transmit Field Optimization 19
Three-Dimensional Density Adapted Projection Reconstruction (3D-DAPR) 19
Transmit Field Mapping: Phase Sensitive Method 20
Three-Dimensional Dictionary Learning Compressed Sensing (3D-DLCS) Reconstruction Algorithm 20
In Vivo Experiments 21
Results 23
In Vivo Sodium (^{23}Na) Magnetic Resonance Imaging of the Human Eye 23
Radio Frequency Coil Design 23
Radio Frequency Coil Performance 25
Electromagnetic Field and Specific Absorption Rate Simulations 26
Transmit Field Mapping 28
In vivo Feasibility Study 30
Application of 3D-DLCS 33
In Vivo Potassium (^{39}K) Magnetic Resonance Imaging of the Human Heart 35
Radio Frequency Coil Design 35
Radio Frequency Coil Performance 37
Electromagnetic Field and Specific Absorption Rate Simulations 38
In Vivo Feasibility Study 39
Discussion 42
References 48
Eidesstattliche Versicherung 52
Anteilserklärung an den erfolgten Publikationen 53
Publications 59
Curriculum Vitae 83

List of publications 87
Acknowledgements 90

List of Figures

Figure 1: (A) Multipurpose interface box which supports ^{23}Na and^{1}H imaging at 7.0 Tesla. (D) Six-way RF power divider using Wilkinson approach for ^{23}Na resonant frequency (f_{23Na}=78.6 MHz). Three boxes (C) contain: one T/R switch (f_{39K}=13.9 MHz), eight T/R switches (four of which were used in our study; f_0=297.2 MHz) and four-way RF power divider (f_{1H}=297.2 MHz).

Figure 2: Left: A view obtained from the CST Studio 2015 illustrating the head of the human voxel model Duke together with the proposed 6-channel transceiver RF array. Red arrows represent discrete ports used for the EMF simulations. Right: The schematic of the 6-channel transceiver RF array. Every channel was tuned to the resonant frequency with a tuning capacitor (C_{Ti}, i={1,…,6}) and matched to the 50 Ω impedance with a matching capacitor (C_{Mi}, i={1,…,6}). Trimmer capacitors were used to decouple element 1 and element 2 (C_{D12}) as well as elements 2 and 3 (C_{D23}). Due to the symmetry of the circuit, the same method was applied to decouple elements 4 and 5 and elements 5 and 6. Inductors used for decoupling of channels: 1 and 3, 4 and 6, and 3 and 6, are denoted as: L_{D13}, L_{D46} and L_{D36}. Inductors L_{D13} and L_{D46} were built as two-turn solenoids and inductors L_{D36} were built as a one-turn solenoid (wire thickness = 1 mm, inner diameter = 6 mm). Their inductances were slightly modified during the process of tuning and matching in order to reduce coupling to an acceptable level.

Figure 3: (A) The final version of the RF circuit illustrated in Fig. 2: copper loops soldered together with capacitors, inductors, cables and cable traps (wrapped with blue rubber). The whole structure is placed on the casing's bottom part and shown with the upper part of the casing next to it. (B) The array placed on the face of a volunteer. (C) ^{23}Na six channel transceiver RF array placed on the cylindrical phantom. This set-up was used for the validation of the transmit field simulations. (D) ^{23}Na/^{1}H imaging set-up: a volunteer together with the ^{23}Na six channel transceiver RF array inside the ^{1}H volume coil.

Figure 4: S-Parameter matrix averaged over 9 volunteers. Averaged values for reflection coefficients were found to be: -19.8 dB for S_{11}, -24.2 dB for S_{22}, -22.5 dB for S_{33}, -21.5 dB for S_{44}, -25.0 dB for S_{55}, -20.1 dB for S_{66}. The highest coupling occurs between elements 2/6 and between loop-elements which were capacitively decoupled: 2/3 and 4/5.

Figure 5: Transmit field (B_1^+) distribution for the phase-optimized setting (PO, channel 1: 0°, channel 2: -202°, channel 3: -186°, channel 4: -282°, channel 5: -246°, channel 6: -279°) in the sagittal, the coronal and the axial plane for human voxel models: Ella (top row) and Duke (bottom row). The red contours represent ROI covering the left and right eye which was used for estimation of B_1^+ homogeneity. It contains all tissues which are considered in the voxel model to belong to the eye: the vitreous humor, the sclera, the cornea and the lens. The black contours represent the extended mask which was provided an error margin and was used for the transmit field optimization.

Figure 6: SAR_{10g} distribution for human voxel models Duke (left) and Ella (right) shown in 3D (top row) and for an axial view through the center of the eyes (bottom row). SAR_{10g} distributions were scaled to the maximum SAR_{10g} value for Duke (0.61 W/kg) in order to highlight good qualitative and quantitative (0.54 W/kg maximum SAR_{10g} value for Ella) agreement between SAR distributions for both human voxel models. The RF chain (its S-Matrix was measured by using a network analyzer) was included in the SAR simulations. Differences in SAR values arise from the anatomical differences between both models (mainly due to variations in shape of the skull and the nose).

Figure 7: (A) Simulated (left) and measured (right) B_1^+ field distribution in a central axial slice of the cylindrical phantom. B_1^+ field was measured by using a phase-sensitive method. Two images with nominal flip angle FA = 90° were acquired: one with the non-selective composite pulse [$2\alpha_0$ α_{90}] and the other one with the first sub-pulse reversed in sign [$2\alpha_{180}$ α_{90}]. Pulse duration was 500 µs. The following parameters were used: TR= 160 ms, TE = 0.5 ms, number of projections = 15000, radial samples = 732, max gradient amplitude = 4 mT/m, max gradient slew rate = 170 mT/m/s, nominal isotropic resolution = 3.0 x 3.0 x 3.0 mm^3, pulse reference amplitude = 75 V. Flip angle maps were normalized to the RF input power. Four different profiles (I, II, III and IV) were drawn in both pictures. Light green color represents profiles for the simulated B_1^+ map and red color represents profiles for the measured B_1^+ map. (B) Quantitative comparison between all simulated and measured profiles. Simulated and measured data show very good agreement.

Figure 8: *In vivo* ^{23}Na image of the eyes of a healthy male volunteer (age = 26 years; BMI = 27.1 kg/m^2) obtained with DA-3DPR imaging and filtered with Hamming filter demonstrated in sagittal and axial view. No method for sensitivity correction was applied. First row: nominal isotropic resolution = 1.4 x 1.4 x 1.4 mm^3 was achieved within 10 minutes 50 seconds using following parameters: TR/TE = 13/0.55 ms, number of projections = 50000, readout duration

= 9.2 ms. Second row: nominal isotropic resolution = 1.0 x 1.0 x 1.0 mm^3 was achieved within 14 minutes 10 seconds by using following parameters: TR/TE = 17/0.55 ms, number of projections = 50000, readout duration = 13.3 ms. Third row: nominal isotropic resolution = 1.0 x 1.0 x 1.0 mm^3 was achieved within 10 minutes 50 seconds by using following parameters: TR/TE = 13/0.55 ms, number of projections = 50000, readout duration = 9.3 ms. Bottom row: proton reference images obtained with ^1H basic coil (Siemens, Erlangen, Germany) and T_2-weighted RARE imaging: TR/TE = 2940/74 ms, FOV = 384 x 384 mm^2, in-plane resolution = 0.54 x 0.54 mm^2, FA = 120°.

Figure 9: *In vivo* ^{23}Na image of the eyes of a healthy female volunteer (age = 29 years; BMI = 19.2 kg/m^2) obtained using the same pulse sequence parameters, imaging protocol and procedure as for the male volunteer shown in Figure 8.

Figure 10: *In vivo* ^{23}Na image of the eyes of a healthy male volunteer (age = 53 years; BMI = 23.5 kg/m^2) obtained with an isotropic spatial resolution of 3 mm (top), 1.4 mm (middle) and 1.0 mm (bottom). A comparison between the low resolution data (3 mm isotropic) and the high resolution data (1.4 and 1.0 mm isotropic) facilitated by the performance gain of the proposed transceiver array underscores the need for enhanced spatial resolution to delineate all of the most important eye compartments.

Figure 11: Comparison of images which resulted from using two different protocols: (A) $N_{averages}$ = 1, $N_{projections}$ = 50000 and (B) $N_{averages}$ = 5, $N_{projections}$ = 10000. Images were reconstructed with non-uniform fast Fourier transform (NUFFT) (top row) and with 3D dictionary learning compressed sensing (3D-DLCS) algorithm (bottom row). The image in bottom row (right) was obtained using only 4 averages what can be used in order to decrease scan time by about 3 minutes without losing fine details which are still present in the image.

Figure 12: (A) Schematic of the proposed $^{39}K/^1H$ RF coil. The pair of ^{39}K Helmholtz loops are highlighted in green. Each loop is split equally by five capacitors C_H. The whole structure was tuned to the resonant frequency of 13.8 MHz and matched to 50 Ω using a balanced configuration. It is also equipped with one cable trap tuned to the resonant frequency of ^1H. The ^{39}K coil is connected through one T/R switch to the MR system. The four-channel ^1H transceiver array is in black. It was equally split with capacitors C_A (anterior part) and C_P (posterior part). The adjacent elements were decoupled using capacitor C_{DCPL}. Each of the elements was tuned to the resonant frequency of 297.2 MHz and matched to 50 Ω using a

balanced configuration. Each channel was equipped with two cable traps tuned both resonant frequencies. (B) The RF signal was divided by using Wilkinson splitter and connected to the T/R switch box through phase cables which supported CP mode. (C) S-Parameter matrix averaged over 8 volunteers is shown for both resonant frequencies (13.9 and 297.2 MHz). Coupling between both coils was weaker at the lower frequency (S_{15} = -49.5 dB, S_{25}= -34.6 dB, S_{35}= -33.4 dB, S_{45}= -35.3 dB) than at the higher frequency (S_{15} = -21.8 dB, S_{25}= -29.3 dB, S_{35}= -23.4 dB, S_{45}= -33.0 dB). Averaged values for reflection coefficients (297.2 MHz) were: -18.2 dB for S_{11}, -24.2 dB for S_{22}, -22.8 dB for S_{33}, -23.7 dB for S_{44}. The capacitive decoupling for the anterior part of the RF coil yielded S_{12} = -12.5 dB, and S_{23} = 16.0 dB for the posterior part.

Figure 13: The proposed $^{39}K/^{1}H$ RF coil placed on a mannequin without (A) and with (B) upper part of the casing.

Figure 14: Transmit field (B_1^+) distribution for an axial cardiac plane of the human voxel models Duke (left) and Ella (right), for the resonant frequencies: 13.9 MHz (^{39}K, top row) and 297.2 MHz (^{1}H, bottom row). The black contours represent the anatomic features including the heart which is localized off-center. Based on qualitative assessment, the ^{39}K Helmholtz loops provide good B_1^+ homogeneity. The CP mode applied for the four-channel ^{1}H array provides fairly constructive B_1^+ interference for whole heart coverage.

Figure 15: SAR_{10g} distribution for both resonant frequencies (13.9 and 297.2 MHz) for both human voxel models Duke and Ella shown in 3D. SAR_{10g} distributions were scaled to the maximum SAR_{10g} value for Ella (0.23 W/kg at 13.9 MHz) in order to highlight good qualitative and quantitative (0.21 W/kg maximum SAR_{10g} value for Duke) agreement between SAR distributions for both human voxel models. The maximum SAR_{10g} values obtained at 297.2 MHz were scaled to the maximum SAR_{10g} for Duke (0.46 W/kg at 297.2 MHz) which was slightly higher than for Ella (0.37 W/kg). A hotspot on the back of Duke at 13.9 MHz results from close vicinity of vertebral disc with respect to the conductive element of the RF coil. In case of Ella, the vertebral disc is located further away from the coil.

Figure 16: Left column: ^{1}H images of the heart obtained from a healthy male volunteer (age = 27 years; BMI = 27.1 kg/m^2) by using following parameters: TE/TR = 2.67/5.66 ms, FOV = (360 x 291) mm^2, in-plane resolution = (1.4 x 1.4) mm^2, slice thickness = 4.0 mm, flip angle = 32°, acquisition time = 12 s. Middle column: *in vivo* ^{39}K images of the same volunteer obtained

using DA-3DPR imaging; filtered with Hamming filter and four-time zero filling and demonstrated in short axis (SAX), four-chamber (4CV), three-chamber (3CV) and two-chamber (2CV) view. The images were acquired with nominal isotropic resolution = 14.5 x 14.5 x 14.5 mm^3 within 30 minutes by using following parameters: TR/TE = 30/0.7 ms, number of projections = 20000, readout duration = 5 ms. Right column: overlay of ^{39}K and ^{1}H images.

Figure 17. *In vivo* ^{39}K MR images, shown in axial view, obtained from six healthy volunteers: four male (MV1, MV2, MV3, MV4) and two female (FV1, FV2), using the same imaging technique as in Figure 16, but different MR system (Terra, Siemens Healthineers, Erlangen, Germany).

Synposis

Abstract

Sodium (Na^+) and potassium (K^+) ions play key roles in the physiology and metabolism of living cells. Primary active transport, which is carried out by sodium/potassium pumps (Na^+/K^+-ATPase), maintains the ion concentration gradient between intra- and extracellular space. Changes in Na^+ and K^+ concentration (and distribution) might reflect ongoing pathological processes within a tissue what might be relevant for various types of cardiovascular and ocular disorders.

Ultrahigh magnetic resonance imaging (UHF-MRI) provides new opportunities to non-invasively investigate changes in Na^+ and K^+ concentrations with spatial resolution and within total scan times that are reaching ranges acceptable for clinical applications. Despite an intrinsic to UHF-MRI gain in signal-to-noise ratio (SNR), nuclear magnetic resonance (NMR) signals of sodium (^{23}Na) and potassium (^{39}K) being detected remain very weak. The NMR sensitivity of ^{23}Na is about 9%, while ^{39}K is 0.05% the one of proton (^{1}H). Therefore, radio frequency (RF) coils, which are used to capture these signals, should be optimized for a given anatomical structure in order to improve the SNR.

The goal of this work is to develop two separate RF coils which would enable high-resolution *in vivo* ^{23}Na MRI of the human eye and *in vivo* ^{39}K MRI of the human heart at 7.0 Tesla. To achieve these goals, the six-channel transmit receive ^{23}Na coil array and a four/two-channel $^{1}H/^{39}K$ coil array have been designed, built and tested. The performance of the developed RF coils has been evaluated using RF circuit, electromagnetic field (EMF) and specific absorption rate (SAR) simulations. Phantom as well as *in vivo* experiments involving several healthy volunteers have been conducted.

The experiments have revealed that the developed six-channel transmit/receive coil array supports *in vivo* ^{23}Na MRI of the human eye with nominal spatial resolution of (1.0 x 1.0 x 1.0) mm^3 and within scan time of 10 minutes. This work also demonstrates that the proposed four/two-channel $^{1}H/^{39}K$ coil array enabled obtaining the world's first *in vivo* ^{39}K image of the human heart with nominal spatial resolution of (14.5 x 14.5 x 14.5) mm^3 and within total scan time of 30 minutes.

The results demonstrate that sodium content in the lens is distinguishable from sodium content in the aqueous and vitreous humor. There is strong evidence that sodium concentration in the compartments of the eye should change in diseases like cataract,

glaucoma and ocular melanoma. The broad roles of this element in processes related to eye physiology suggest a range of questions for ophthalmological investigations. This work also shows that *in vivo* potassium MRI of the human heart is feasible. Previous reports, suggesting that potassium concentration is expected to alter in arrhythmia, ischemia or irreversible injury to miocytes, provides encouragement for future *in vivo* studies involving patients who suffer from various cardiovascular disorders.

Abstrakt

Natrium- (Na^+) und Kaliumionen (K^+) spielen kritische Rollen in der Physiologie und dem Metabolismus lebender Zellen. Der primär-aktive Transport, der den Ionenkonzentrationsgradienten zwischen intra- und extrazellulärer Maxtrix aufrecht hält, wird von Natrium/Kaliumpumpen durchgeführt. Änderungen der Na^+ - und K^+-Konzentration und -Verteilung könne auf pathologische Prozesse in einem Gewebe zurückzuführen sein. Dies ist sehr relevant für eine Vielzahl von Krankheiten, einschließlich Herz-Kreislauf- und Augenerkrankungen.

Ultrahohe Magnetresonanztomographie (UHF-MRT) bietet neue Möglichkeiten zur nicht-invasiven Untersuchung von Änderungen in Na^+- und K^+-Konzentrationen mit hoher räumlicher Auflösung, die innerhalb für klinische Anwendungen akzeptabler Gesamtabtastzeiten durchgeführt werden können. Trotz eines UHF-MRT-spezifischen Anstiegs des Signal-Rausch-Verhältnisses (SNR) bleiben die nachgewiesenen kernmagnetischen Resonanzsignale (NMR) von Natrium (^{23}Na) und Kalium (^{39}K) sehr schwach. Die NMR-Empfindlichkeit von ^{23}Na beträgt etwa 9%, während ^{39}K - 0.05% des Protons (^{1}H) beträgt. Daher sollten Hochfrequenzspulen (HF), die zur Erfassung dieser Signale verwendet werden, für eine bestimmte anatomische Struktur optimiert werden, um das SNR zu verbessern.

Ziel dieser Arbeit ist es, zwei separate HF-Spulen zu entwickeln, die eine hochauflösende *in vivo* ^{23}Na-MRT des menschlichen Auges und eine *in vivo* ^{39}K-MRT des menschlichen Herzens bei 7.0 Tesla ermöglichen. Um diese Ziele zu erreichen, wurden das/ein ^{23}Na-Spulenarray mit sechs Sende- und Empfangskanälen und ein $^{1}H/^{39}K$-Spulenarray mit vier/zwei Kanälen entworfen, gebaut und getestet. Es wurden Experimente an Messphantomen sowie *In-vivo*-Testmessungen von mehreren gesunden Freiwilligen durchgeführt.

Die Messungen haben gezeigt, dass das in dieser Arbeit entwickelte 6-Kanal-Sende- / Empfangsspulenarray *in vivo* ^{23}Na MRT des menschlichen Auges mit einer nominalen räumlichen Auflösung von (1.0x1.0x1.0) mm^3 innerhalb der Scanzeit von 10 Minuten ermöglicht. Diese Arbeit zeigt auch, dass es dank des $^{1}H/^{39}K$ -Spulenarray mit vier/zwei Kanälen gelang, das weltweit erste ^{39}K -Bild des menschlichen Herzens *in vivo* mit einer nominalen räumlichen Auflösung von (14.5x14.5x14.5) mm^3 und einer Gesamtabtastzeit von zu 30 Minuten aufzunehmen.

Die Ergebnisse zeigen, dass der Natriumgehalt in der Linse vom Natriumgehalt im wässrigen und im Glaskörper unterscheidbar ist. Es gibt starke Hinweise darauf, dass sich die

Natriumkonzentration in den Kompartimenten des Auges bei Erkrankungen wie Katarakt, Glaukom und okularem Melanom ändern sollte. Diese Arbeit zeigt auch, dass eine in vivo Kalium-MRT des menschlichen Herzens möglich ist. Frühere Berichte, aus denen hervorgeht, dass sich die Kaliumkonzentration voraussichtlich bei Arrhythmie, Ischämie oder irreversiblen Verletzungen der Miozyten ändert, ermutigen zukünftige *In-vivo*-Studien mit Patienten, die an verschiedenen Herz-Kreislauf-Erkrankungen leiden.

Introduction

Magnetic resonance imaging (MRI) is probably the most powerful and versatile, non-invasive, diagnostic technique used in modern medicine. Typical anatomical MRI scans are based on detection of the nuclear magnetic resonance (NMR) signal from protons (^{1}H). However, other atomic nuclei in humans could potentially be imaged using MR. Such nuclei are generally present in very low quantities, and their physical properties like nuclear spin number or gyromagnetic ratio are less advantageous compared to ^{1}H. These factors have a major impact on the signal-to-noise ratio (SNR) that can be achieved, which consequently limits the spatial resolution of an MR image and prolongs the total acquisition time that is required. The SNR increases supralinearly with the applied static magnetic field strength (B_0). Therefore, ultrahigh field ($B_0 \geq 7T$) magnetic resonance imaging (UHF-MRI) can provide benefits in non-proton nuclei (X-nuclei) imaging. This has brought *in vivo* imaging of nuclei such as sodium (^{23}Na) and even potassium (^{39}K) within ranges of spatial resolution and scan time which might be encouraging for clinical applications. The potential to image ^{23}Na and ^{39}K by non-invasive means might be of high clinical relevance and yield unique types of diagnostic information fundamentally different from that obtainable through typical ^{1}H scans.

The sodium and potassium isotopes ^{23}Na and ^{39}K appear in the human body as sodium (Na^+) and potassium (K^+) cations which play crucial roles in human physiology and metabolism [1]. These include functions in determining the composition of the cytoplasm of cells, in transporting molecules through cell membranes, propagating action potentials (e.g. neurons, myocytes), and controlling cell volume and pH.

Na^+ is mainly concentrated in the extracellular matrix ($[Na^+]_{ext} \approx 140$ mM), while K^+ is largely intracellular ($[K^+]_{int} \approx 140$ mM). The concentration gradient across cell membranes is governed by the activity of sodium/potassium pumps (Na^+/K^+-ATPase). Sodium plays a critical role in this context, since its main function is the storage of chemical energy obtained through the hydrolysis of one molecule of adenosine triphosphate (ATP) per one turnover of a pump. This energy is used to transport three Na^+ across the cell membrane to the extracellular matrix, against the concentration gradient, while two K^+ are transported into the cell. The discovery of this protein was deemed so important that Jens C. Skou was awarded Nobel Prize in chemistry in 1997 for having achieved it [2].

Potassium is not only involved in the function of Na^+/K^+-ATPase, but also in K^+ channels - one of the largest and most functionally-diverse families of ion-channel proteins in the human genome. They are particularly crucial for the electrical excitability of various types of cells. The significance of K^+ channels was also highlighted by a Nobel Prize in chemistry, to Roderick MacKinnon in 2003 for his discoveries in this field [3].

This means that the possibility of probing changes in the distribution and/or concentration of Na^+ and K^+ in a tissue *in vivo* could add a new dimension to our understanding, diagnosis and, potentially, treatment of many diseases. Thus "electrolyte mapping" is on the most promising research areas in the development of UHF-MRI.

Since the earliest days of *in vivo* nuclear magnetic resonance (NMR), potassium has been regarded as an intriguing nucleus to investigate, given its crucial roles in a very broad range of biological processes [4]. Nevertheless, sodium (Na^+) has historically received more attention from the biomedical imaging community, largely because of its high NMR signal *in vivo* – second only to that of protons.

In vivo ^{23}Na MRI has already been carried out by a number of investigators who have successfully applied it in tissues such as the brain, heart, cartilage and skin. *In vivo* ^{23}Na MRI of the human eye, however, is an area that remains completely unexplored. This might seem surprising given sodium's essential roles in the energy-consuming processes of membrane transport that occur in several compartments of the eye. Primary active transport, which is carried out by Na^+/K^+-ATPase, is a major link between processes which occur in the human eye and its compartments. These include the formation of the aqueous humor (crucial in the regulation of intraocular pressure), the maintenance of the Na^+/K^+ gradient between the lens and the vitreous humor, and the removal of water and lactic acid from the retinal pigment epithelium into the blood.

Potassium MRI is much more challenging since its sensitivity is 180 times lower than that of ^{23}Na. With the exception of a few animal studies, the literature presents only three publications on *in vivo* ^{39}K MRI in humans. Umathum et al. [5] investigated human brain and muscle at 7.0 T. This study was followed up by Rosler et al. [6], who reported on quadrupolar splitting of the ^{39}K resonance in skeletal muscle. Atkinson et al. [7] focused on imaging the brain using a magnetic field strength of 9.4 T. The critical role that potassium ions play in cardiac electrophysiology has motivated the author to investigate the more challenging problem of *in vivo* ^{39}K MRI of the human heart, which has not yet been demonstrated.

The significance of *in vivo* explorations into Na^+ and K^+ using MRI arises from the fact that alterations in their distribution and concentration might reflect pathophysiological processes (e.g. impairment of Na^+/K^+-ATPase). This issue has been explored in several diseases using *in vivo* ^{23}Na MRI. It has been demonstrated that the sodium level in a tissue can significantly change in breast and brain tumors, strokes and cartilage diseases [8].

This is also likely to be the case in diverse ocular disorders. Changes in sodium concentrations have been investigated using ^{23}Na MRI in several *ex vivo* studies involving eye tumors and cataracts [9,10]. It is also highly probable that sodium concentration change in some types of glaucoma [11].

Potassium levels are also likely to change during pathological processes in the heart, such as increases in concentrations of extracellular K^+ following ischemia [12] or decreases in tissue K^+ which lead to irreversible injuries to cardiomyocytes [13]. Since potassium is vasoactive and important in regulating smooth muscle tone and blood flow, altered smooth muscle K^+ channel functions are likely to occur in several pathological conditions [14].

The link between these projects on the eye and heart is the growing realization that common mechanisms underlie diseases processes in both cardiovascular and ocular tissues, particularly with regard to aging and chronic conditions such as age-related macular degeneration, glaucoma and diabetic retinopathy [15].

New diagnostic techniques are necessary to pave the way for innovative forms of diagnosis and therapies which would target ocular and cardiovascular disorders (CVD). Glaucoma and cataract are two world leading causes of blindness. Glaucoma affects more than 32 million, while cataract - 95 million people worldwide. CVD's are world leading causes of death and their incidence is estimated to be about 420 million [16].

Low *in vivo* ^{23}Na and, in particular, ^{39}K NMR sensitivity require that special attention be paid in the design of radio frequency (RF) coils. Since the RF coil is a central link in a transmit/receive chain of every MR system, it is important to custom tailor RF technology for a given nucleus and desired anatomical region to maximize the SNR.

Here the author's approach to these problems has been to develop local multi-channel transmit/receive RF coils. There are several motivations for doing so. First of all, smaller (and to a certain extent), independently-driven conductive loops which cover the same human body area as one big conductive loop can provide higher SNR [17].

Secondly, "local" means that such a solution offers benefits for transmission efficiency, i.e., the ratio of transmit field and the square root of applied RF power. When the RF coil is placed closed to the ROI, less RF power is required to achieve the desired flip angle than for an RF coil that is placed further away (as in the extreme case of the body coils used in clinical 1.5 and 3.0 T MR scanners). This is particularly important because the peak RF power supported by the RF amplifier in commercial MRI machines is limited. Transmission efficiency is particularly crucial in experiments involving nuclei such as ^{23}Na and ^{39}K, which have much lower gyromagnetic ratios (γ_{39K} = 1.99 MHz/T, γ_{23Na} = 11.26 MHz/T). In this situation, more RF power is required to achieve the desired flip angle (in case of a commonly used rectangular RF pulse, the flip angle is linearly proportional to the gyromagnetic ratio, transmit field magnitude and RF pulse duration) than in ^{1}H (γ_{1H} = 42.57 MHz/T).

Third, the multi-channel approach permits driving each channel with a different phase. Using special algorithms, the transmit field in the ROI can be optimized in terms of homogeneity and magnitude, while keeping the specific absorption rate (SAR) at the lowest

possible levels for a given coil configuration. What is equally important, but often neglected, is the fact that SAR at lower resonant frequencies (at 7.0 T: f_{39K} = 13.9 MHz and f_{23Na} = 78.6 MHz) might be just as challenging as for nuclei such as ^{1}H (f_{1H} = 297.2 MHz) which have much higher resonant frequencies. SAR is proportional to the square of frequency, but at the same time also to the square of the magnitude of the transmit field. So, even if the resonant frequency for ^{23}Na and ^{39}K is much lower than ^{1}H, this advantage is offset by the higher RF power required to achieve the same flip angle.

Ideally, the RF coil design for X-nuclei imaging should also permit imaging ^{1}H. This would provide an opportunity to obtain anatomical information along with B_0 shimming capabilities.

There is a lack of literature data on *in vivo* ^{23}Na MRI of human eyes using a dedicated RF setup. The only *in vivo* data appears circumstantially in publications on sodium imaging of the human brain at different field strengths: 1.5T [18], 3.0T [1], 4.7 [19], 7.0 T [20], 9.4T [21], because the eyes happen to be within the area captured by scans. The main observation that can be taken from these studies is that the ^{23}Na signal from the eyes, which are prominent in particular slices of the human head, essentially dominates any other signal from the brain, even though suboptimal RF set-ups (in the context of eye imaging) were used for these investigations. Therefore, it is hypothesized that a dedicated local multi-channel array might enable imaging the eye and its substructures with excellent spatial resolution and scan times that have yet to be demonstrated.

Nor has there been a report published on *in vivo* ^{39}K MRI of the human heart. *In vivo* ^{39}K MRI is more challenging than ^{23}Na, not only because of the significantly lower NMR sensitivity, but also because of issues related to respiratory and cardiac motion. Here, the aim is to demonstrate the feasibility of *in vivo* ^{39}K MRI of the human heart and discuss future directions, and whether or not the spatial resolution and total acquisition times that can be achieved are suitable for clinical applications.

In this work, two separate, custom-tailored RF coils have been developed for two different clinical applications: *in vivo* ^{23}Na MRI of human eyes and *in vivo* ^{39}K MRI of human heart at 7.0 T. This work describes the designs of both RF coils and reports on electromagnetic field (EMF) and specific absorption rate (SAR) simulations and phantom measurements. The RF technology developed here has been applied in two separate *in vivo* proof-of-principle studies involving several healthy volunteers.

Methodology

Numerical Electromagnetic Field and Specific Absorption Rate Simulations

The electromagnetic field (EMF) and specific absorption rate (SAR) simulations were performed using the Finite Integration Technique of CST Studio Suite 2015 (CST AG, Darmstadt, Germany) with the human voxel models Duke (male) and Ella (female) from the Virtual Family. SAR is a spatially-dependent ($\vec{r} = x, y, z$) parameter, defined as follows:

$$SAR = \frac{1}{V}\int \frac{\sigma(\vec{r})\left|\vec{E}(\vec{r})\right|^2}{\rho(\vec{r})} d\vec{r} \quad (1)$$

where V is the tissue volume, σ is the electrical conductivity of a tisse, $\vec{E}$ is the electric field and ρ is the tissue density. According to the safety guidelines, averaged local SAR is calculated in a mass volume of 10 g (SAR_{10g}). The electrical properties of all human tissues were altered according to the IT'IS database (IT'IS, Zurich, Switzerland) [22]. The results of the simulations were exported from the CST Studio Suite into the Advanced Design System (ADS) (Keysight EEsof EDA, Keysight Technologies, Santa Rosa, CA, USA). In ADS, a thorough analysis of electrical circuits was conducted. Coupling between all of the elements of the developed radio frequency (RF) coils was analyzed, and capacitive-inductive circuits were designed to reduce it. Capacitors and inductors used in simulations were modeled with additional resistances, which represented typical losses for lumped elements and losses inherent to soldering joints [23]. The input RF power was adjusted to meet the regulations provided by the International Electrotechnical Commission guideline 60601-2-33 Ed.3 [24].

Benchtop Evaluation

The RF coils were evaluated at the bench. The measurements were performed using an eight-channel vector network analyzer (ZVT 8, Rohde & Schwarz, Memmingen, Germany). Scattering parameter matrices (S-Matrix), which mirror inter-element coupling in multi-channel arrays, were measured for both RF coils and for various loading conditions: including nine volunteers (body mass index range: 20.1–27.1 kg/m^2) in case of ^{23}Na RF coil and eight volunteers (BMI range: 18.9 - 28.5 kg/m^2) in case of ^{39}K RF coil. S-Matrices were measured, exported from the network analyzer, and analyzed in MATLAB (The MathWorks, Natick, MA, USA).

Magnetic Resonance Imaging Hardware

Phantom and human imaging studies were conducted on a 7.0 T whole-body system (Magnetom, Siemens Healthcare, Erlangen, Germany), equipped with a gradient system that supported a slew rate of 170 mT/m/ms and a maximum gradient strength of 38 mT/m. For RF transmission, a single-channel RF amplifier (P_{max} = 8 kW, Stolberg HF-Technik AG, Stolberg-Vicht, Germany) was applied. Further in vivo ^{39}K MRI experiments (n=6), were conducted using another 7.0 T whole-body MR system (Terra, Siemens Healthineers, Erlangen, Germany) which supports ^{39}K MRI. This MR system is equipped with a gradient system supporting dG/dt_{max} = 200 mT/m/ms, G_{max} = 80 mT/m.

The multipurpose interface box (MRI.TOOLS GmbH, Berlin, Germany) used for ^{23}Na RF coil consists of 16 transmit/receive (T/R) switches (Figure 1A): 8 for proton (^{1}H) and 8 for ^{23}Na resonant frequency at 7T, along with integrated low-noise preamplifiers (Stark Contrasts, Erlangen, Germany). The single channel ^{23}Na RF signal was split into six channels using a Wilkinson RF power divider shown in Figure 1B.

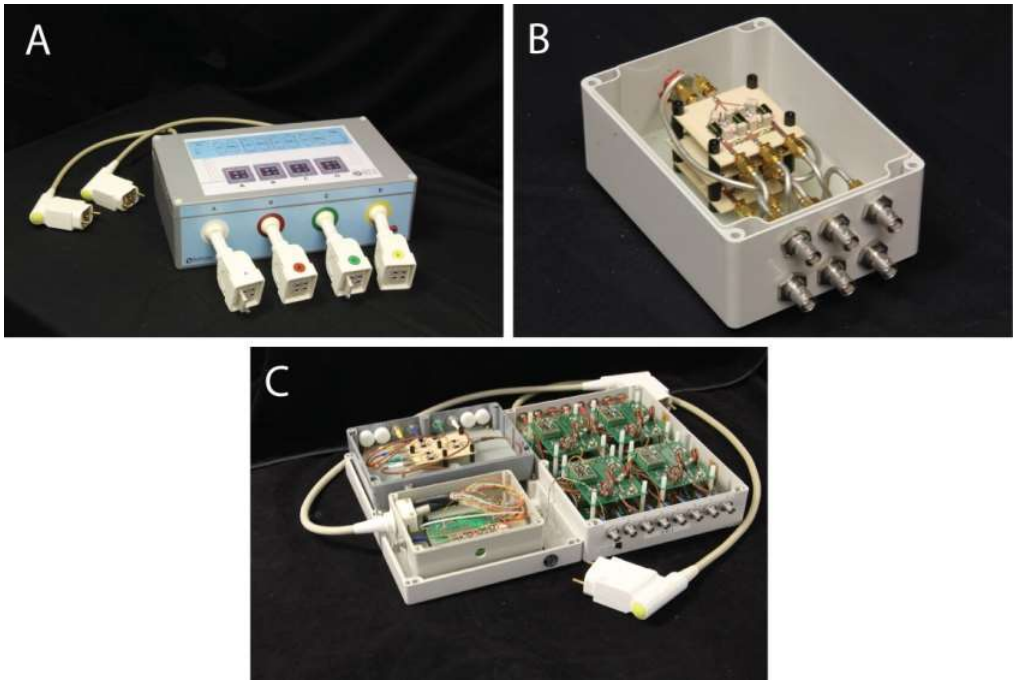

Figure 1: (A) Multipurpose interface box which supports ^{23}Na and^{1}H imaging at 7.0 Tesla. (D) Six-way RF power divider using Wilkinson approach for ^{23}Na resonant frequency (f_{23Na}=78.6 MHz). Three boxes (C) contain: one T/R switch (f_{39K}=13.9 MHz), eight T/R switches (four of which were used in our study; f_0=297.2 MHz) and four-way RF power divider (f_{1H}=297.2 MHz).

The multipurpose interface boxes used to connect the ^{39}K/^{1}H RF coil to the scanner (Figure 1C) consist of four T/R switches for 297.2 MHz and one T/R switch for 13.9 MHz along

with integrated low-noise preamplifiers for each of the resonant frequencies (Stark Contrast, Erlangen, Germany).

Transmit Field Optimization

Transmit field optimization was used to find a trade-off between two major goals: transmit field homogeneity and transmit field efficiency which maximizes B_1^+ amplitude in a region of interest (ROI) while minimizing SAR in both human voxel models. These conditions are included in the following merit function:

$$f(\Phi) = \frac{std(|B_1^+(\Phi)|)}{mean(|B_1^+(\Phi)|)} - \beta * \frac{1}{\sqrt{max\left(SAR_{10g}^{Duke}(\Phi),\ SAR_{10g}^{Ella}(\Phi)\right)}} * \frac{MOS(|B_1^+(\Phi)|)}{SOM(|B_1^+(\Phi)|)} \qquad (2)$$

where β is the weighting factor, and MOS (magnitude of sum) and SOM (sum of magnitudes) are defined as follows:

$$MOS(|B_1^+(\Phi)|) = \left|\sum_i B_1^+(\Phi_i)\right| \quad , \quad SOM(|B_1^+(\Phi)|) = \sum_i |B_1^+(\Phi_i)| \qquad (3)$$

In order to minimize f(Φ), a multi-objective genetic algorithm implemented in MATLAB was used.

Three-Dimensional Density Adapted Projection Reconstruction (3D-DAPR)

^{23}Na and ^{39}K are nuclear spin 3/2 systems. This usually leads to biexponential relaxation in a tissue what results in transverse relaxation time T_2 having two components: slow T_{2s} and fast T_{2f}. Using too long echo times (TE) can lead to a severe signal loss which is related to vanishing of the fast component (even up to 60% signal loss). This is why imaging techniques, which enable applying very short TE, are critical for imaging nuclei with nuclear spin number of 3/2 like sodium and potassium. In this work, three-dimensional density adapted projection imaging (3D-DAPR) was employed [25]. The term “density adapted” stands for more efficient k-space sampling in the k-space center than conventional three-dimensional radial projection reconstruction.

Transmit Field Mapping: Phase Sensitive Method

In order to calculate B_1^+ distribution, the phase-sensitive method, which was introduced by G. Morrell, and additionally incorporated into 3D-DAPR, was used [26]. This method uses 2α RF pulses about the x-axis, followed immediately by an α RF pulse about y-axis (x and y are MR scanner's coordinates). The information about flip angle is then encoded in the signal phase. There are two acquisitions needed in order to cancel out the sources of errors resulting from, e.g. eddy currents. The second acquisition is performed using 2α RF pulse with a negative sign. The phase difference ϑ for on-resonance spins can be calculated from following formula:

$$\vartheta = 2\tan^{-1}\left(\frac{2\cos\alpha}{\cos 2\alpha}\right) \tag{4}$$

Three-Dimensional Dictionary Learning Compressed Sensing (3D-DLCS) Reconstruction Algorithm

MR images are considered compressible just like other types of images such as those in JPEG format. "Compressible", in this context, means that there is a lot of information which is not crucial to fully represent the significant data in a desired way. Compressed sensing is a reconstruction technique, in which first the compressed information is "sensed" directly by making fewer measurements, instead of acquiring full information which later can be compressed [27]. There are two conditions to be fulfilled in order to use compressed sensing: an image must have a sparse representation in some domain, and data sampling must be performed by pseudo-random or non-uniform means (undersampling artifacts must be incoherent). Then, a non-linear reconstruction algorithm is necessary to solve a set of nonlinear underdetermined equations.

In this work a 3D-dictionary learning compressed sensing (3D-DLCS) reconstruction algorithm, which is tailored for the 3D-DAPR imaging technique, was applied [28]. The main task of 3D-DLCS algorithm is to solve iteratively the following problem:

$$\left\{\widehat{\mathrm{D}},\widehat{\alpha}_{\mathrm{ijk}},\widehat{\mathrm{X}}\right\} = \mathrm{argmin}_{\mathrm{D},\alpha_{\mathrm{ijk}},\mathrm{X}} \sum_{\mathrm{ijk}} \mu_{\mathrm{ijk}}\left\|\alpha_{\mathrm{ijk}}\right\|_0 + \sum_{\mathrm{ijk}}\left\|\mathrm{D}\alpha_{\mathrm{ijk}} - \mathrm{R}_{\mathrm{ijk}}\mathrm{X}\right\|_2^2 + \lambda\|\mathrm{FX} - \mathrm{Y}\|_2^2 \tag{5}$$

where X is the reconstructed image, F is the non-uniform fast Fourier transform (NUFFT) operator, Y is the measured raw data, α_{ijk} is the sparse representation in the dictionary D, and R_{ijk} is a diagonal matrix that extracts the blocks of interest from the image. The cost function

combines the sparsity of the dictionary coefficients through $\sum_{ijk} \mu_{ijk} \left\| \alpha_{ijk} \right\|_0$, block-wise consistency of the reconstructed image and its dictionary representation through $\sum_{ijk} \left\| D\alpha_{ijk} - R_{ijk}X \right\|_2^2$ and data consistency of the reconstructed image through $\lambda \| FX - Y \|_2^2$.

In Vivo Experiments

Sodium MRI was performed in seven healthy adult volunteers (3 female: mean age = 28.5 years, mean BMI = 22.0 kg/m^2; 4 male: mean age = 33.5 years, mean BMI = 23.9 kg/m^2). The parameters of 3D-DAPR sequence were chosen as follows:

a) For a nominal isotropic resolution of 1.4 x 1.4 x 1.4 mm^3: TR = 13 ms; TE = 0.55 ms; nominal FA = 41°; number of projections = 50000; readout duration = 9.2 ms; radial samples = 520; maximum gradient amplitude = 18 mT/m; maximum gradient slew rate = 170 mT/m/s; pulse reference amplitude = 200 V. The acquisition time was 10 minutes 50 seconds.

b) For a nominal isotropic resolution of 1.0 x 1.0 x 1.0 mm^3: TR = 17 ms; TE = 0.55 ms; nominal FA = 41°; number of projections = 50000; readout duration = 13.3 ms; radial samples = 864; maximum gradient amplitude = 22 mT/m; maximum gradient slew rate = 170 mT/m/s; pulse reference amplitude = 200 V. The acquisition time was 14 minutes 10 seconds.

c) For a nominal isotropic resolution of 1.0 x 1.0 x 1.0 mm^3: TR = 13 ms; TE = 0.55 ms; nominal FA = 41°; number of projections = 50000; readout duration = 9.3 ms; radial samples = 864; maximum gradient amplitude = 25 mT/m; maximum gradient slew rate = 170 mT/m/s; pulse reference amplitude = 200 V. The acquisition time was 10 minutes 50 seconds

Ophthalmological ^{1}H imaging was performed to obtain an anatomical reference image, employing a T_2-weighted 2D Rapid Acquisition with Relaxation Enhancement (RARE) technique (TR = 2940 ms; TE = 74 ms; spatial resolution = 0.54 x 0.54 mm^2; FOV = 384 x 384 mm^2; number of slices = 3; slice thickness = 1.4 mm; nominal refocusing FA = 120°, NA = 1. The acquisition time was 1 minute 8 seconds.

Proof-of-principle in vivo ^{39}K MRI was performed in seven healthy subjects (5 male, 2 female; average BMI = 24.1 kg/m^2, average age = 34 years) with 3D-DAPR imaging technique: TR = 30 ms; TE = 0.7 ms; number of projections = 20000; read-out duration = 5 ms; maximum gradient amplitude = 11.95 mT/m, slewrate = 170 T/(m·s), beginning of the density-adapted part at t0 = 0.5 ms, rectangular pulse duration = 1 ms; radial samples = 64; dwell time = 78.1 µs; nominal isotropic resolution = (14.5x14.5x14.5) mm^3. The acquisition time was 30 minutes. The RF coil and receiver chain do not support simultaneous ^{39}K/^{1}H imaging.

For ^{1}H CINE imaging of the heart two (2CV), three (3CV), four chamber (4CV) and short axis (SAX) views were acquired using breath-hold 2D CINE FLASH (TE = 2.67 ms, TR = 5.66 ms, matrix size = 256 x 256, FOV) = (360 x 291) mm^2, in-plane spatial resolution = (1.4x1.4) mm^2, slice thickness = 4.0 mm, flip angle = 32°, receiver bandwidth = 444 Hz/pixel, acquisition time = 12 s.

Results

In Vivo Sodium (^{23}Na) Magnetic Resonance Imaging of the Human Eye

Partial results of the work, which are presented in this chapter, have been published in:

D. Wenz, A. Kuehne, T. Huelnhagen, A.M. Nagel, H. Waiczies, O. Weinberger, C. Oezerdem, O. Stachs, S. Langner, E. Seeliger, B. Flemming, R. Hodge, T. Niendorf, "Millimeter Spatial Resolution In Vivo Sodium MRI of the Human Eye at 7 T Using a Dedicated Radiofrequency Transceiver Array", *Magnetic Resonance in Medicine* 2018 Aug;80(2):672-684. doi: 10.1002/mrm.27053.

Radio Frequency Coil Design

The proposed radio frequency (RF) coil array consists of six loop-elements and is symmetrically divided into two sections. Each section is composed of three loop-elements which were angled to each other in order to conform to the anterior part of an average human head as demonstrated in Figure 2. The size of a single element (36 x 71 mm) was chosen to achieve sufficient RF penetration depth [29] for eye imaging. The shape and the surface area of an average human head limit the number of elements per eye. Applying more than three elements per eye does not improve the RF coil's performance, because they would be already too far from the ROI. Two more elements (one per eye) could be added from the top, but they would couple strongly with all of the other loops. Offsetting the extra coupling would require more decoupling circuits (resulting in increased losses) so that the total weight would increase and cause more patient discomfort without any gain in performance. The arrangement of element 1 (or element 4) versus element 2 (or element 5) was obtained by applying an inclination angle of 151°. In order to arrange element 2 (or element 5) versus element 3 (or element 4), an angle of 161° was applied. The six-channel array is made up of four loops of rectangular shape (elements 1, 2, 4, 5) and two of polygonal shape (elements 3 and 6). The polygonal loops are designed to fit the space around the nose in a way that permits bilateral vision through them (Figure 3A). To achieve a sufficient RF field penetration depth, the height of a single loop was set at 71 mm and its width at 36 mm. The width of the conductor was 10 mm.

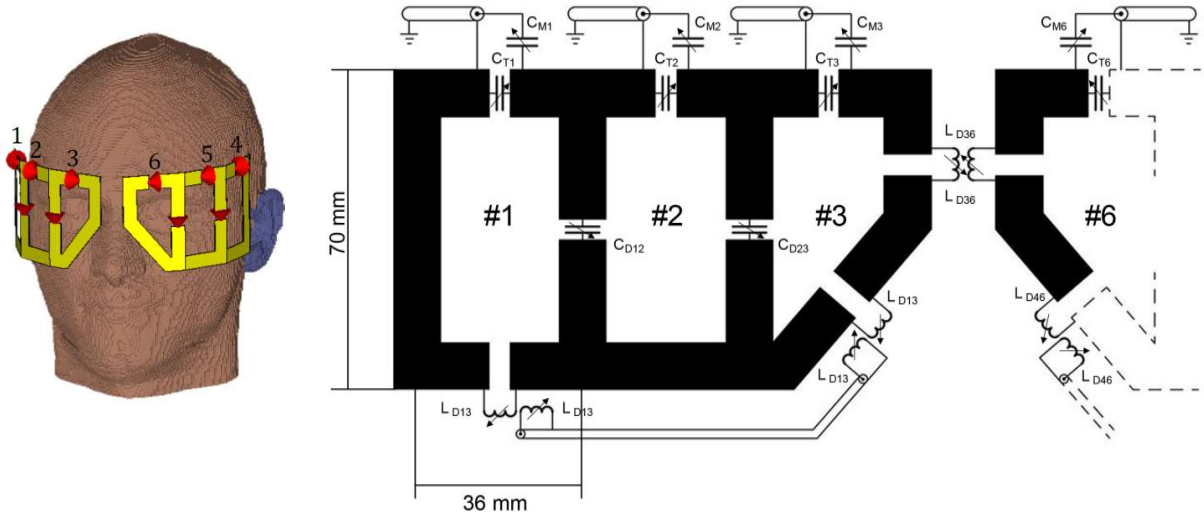

Figure 2: Left: A view obtained from the CST Studio 2015 illustrating the head of the human voxel model Duke together with the proposed 6-channel transceiver RF array. Red arrows represent discrete ports used for the EMF simulations. Right: The schematic of the 6-channel transceiver RF array. Every channel was tuned to the resonant frequency with a tuning capacitor (C_{Ti}, i={1,…,6}) and matched to the 50 Ω impedance with a matching capacitor (C_{Mi}, i={1,…,6}). Trimmer capacitors were used to decouple element 1 and element 2 (C_{D12}) as well as elements 2 and 3 (C_{D23}). Due to the symmetry of the circuit, the same method was applied to decouple elements 4 and 5 and elements 5 and 6. Inductors used for decoupling of channels: 1 and 3, 4 and 6, and 3 and 6, are denoted as: L_{D13}, L_{D46} and L_{D36}. Inductors L_{D13} and L_{D46} were built as two-turn solenoids and inductors L_{D36} were built as a one-turn solenoid (wire thickness = 1 mm, inner diameter = 6 mm). Their inductances were slightly modified during the process of tuning and matching in order to reduce coupling to an acceptable level.

The elements for this design were manufactured from 36 μm copper on a 0.5 mm FR-4 substrate using a CNC machine (ProtoMat, LPKF Laser & Electronics AG, Garbsen, Germany). Adjacent loops (elements 1/2; elements 2/3; elements 6/5 and elements 5/4), which share common conductors, were capacitively decoupled. Non-adjacent loops (elements 1/3; elements 6/4) were inductively decoupled, as were the two loops around the nose (elements 3/6). The capacitive decoupling was achieved using chip ceramic capacitors (American Technical Ceramics Inc, Huntington Station, NY, USA) along with trimmer capacitors (Voltronics Inc, MD, USA). Inductive decoupling was accomplished using inductors (inner diameter – 6 mm, wire thickness – 1 mm) covered by a thin layer of insulation. In order to facilitate inductive decoupling between non-adjacent elements, two small pieces of coaxial cable were used to close the circuits as illustrated in Figure 3A. Cable traps were placed 10 cm away from the coil to eliminate common mode currents. They were built from a wound cable and a capacitor which was soldered to the outer shield of the cable. The coil casing was designed by using Autodesk Inventor Professional 2013 (Autodesk Inc, San Rafael, CA), and was constructed from ABS material using 3D printer (BST 1200es; Dimension Inc, Eden

Prairie, MN). The dimensions of the proposed array conform to an average human head (Figure 3B) and to the phantom used for validation of the simulations (Figure 3C) and). A commercial volume coil (inner diameter = 34 cm), which is circularly polarized birdcage coil, was used to obtain anatomical reference image (Figure 3D).

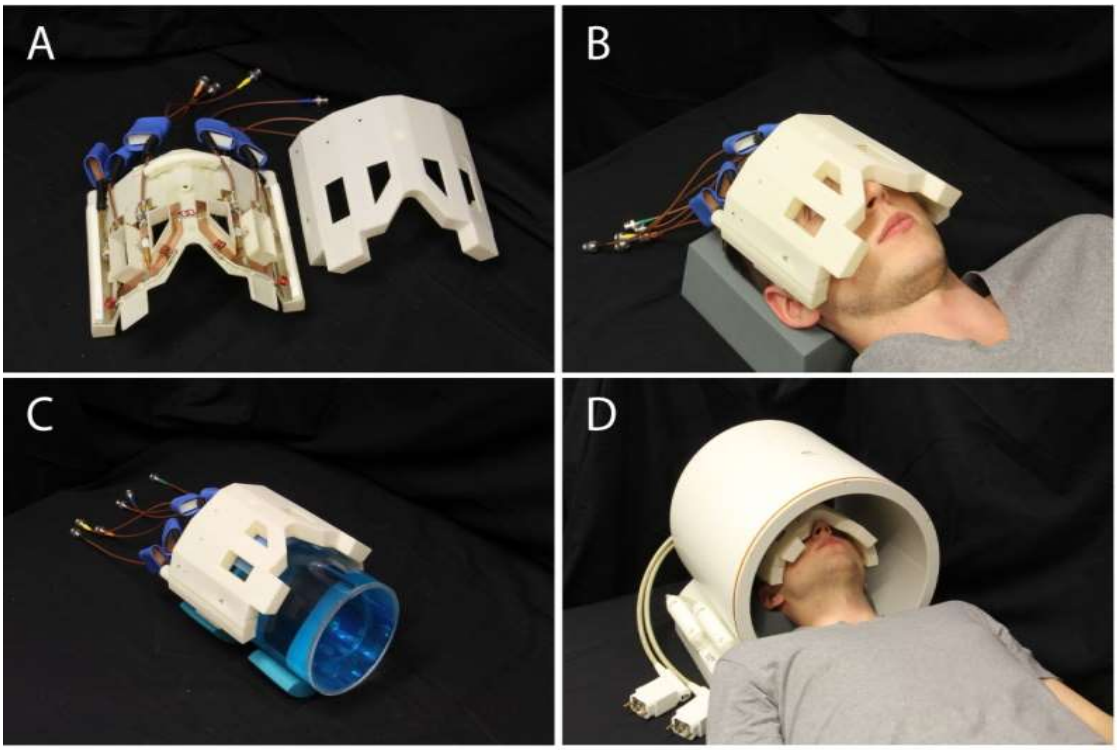

Figure 3: (A) The final version of the RF circuit illustrated in Fig. 2: copper loops soldered together with capacitors, inductors, cables and cable traps (wrapped with blue rubber). The whole structure is placed on the casing's bottom part and shown with the upper part of the casing next to it. (B) The array placed on the face of a volunteer. (C) ^{23}Na six channel transceiver RF array placed on the cylindrical phantom. This set-up was used for the validation of the transmit field simulations. (D) ^{23}Na/^{1}H imaging set-up: a volunteer together with the ^{23}Na six channel transceiver RF array inside the ^{1}H volume coil.

Radio Frequency Coil Performance

The measured S-Matrix averaged over 9 volunteers (5 men and 4 women) is demonstrated in Figure 4. S_{11} values for all volunteers were found between -17.0 and -21.5 dB, S_{22} between -18.7 and -38.2 dB, S_{33} between -17.1 and -26.0 dB, S_{44} between -13.1 and -34.3 dB, S_{55} between -12.4 and -36.7 dB and S_{66} between -12.0 and -28.3 dB. Applying capacitive decoupling between elements 1 and 2 (and due to the symmetry of the circuit, between 4 and 5) and between 2 and 3 (or 5 and 6) yielded averaged transmission coefficient values of -16.4 dB for S_{12} (-14.0 dB for S_{45}) and -13.1 dB for S_{23} (-16.8 dB for S_{56}). Applying

inductive decoupling between elements 1 and 3 (4 and 6) gave -17.8 dB for S_{13} (-17.7 dB for S_{46}) and between elements 3 and 6: -19.1 dB for S_{36}. The cylindrical phantom was used in order to evaluate the Q_{UL}/Q_L ratio for each loop element of the array. The measurements yielded the Q_{UL}/Q_L ratio as follows: element 1 – 1.8, element 2 – 2.1, element 3 – 1.3, element 4 – 1.7, element 5 – 1.6, element 6 – 1.3. The average Q factor value for all of the loops was estimated to be 1.6.

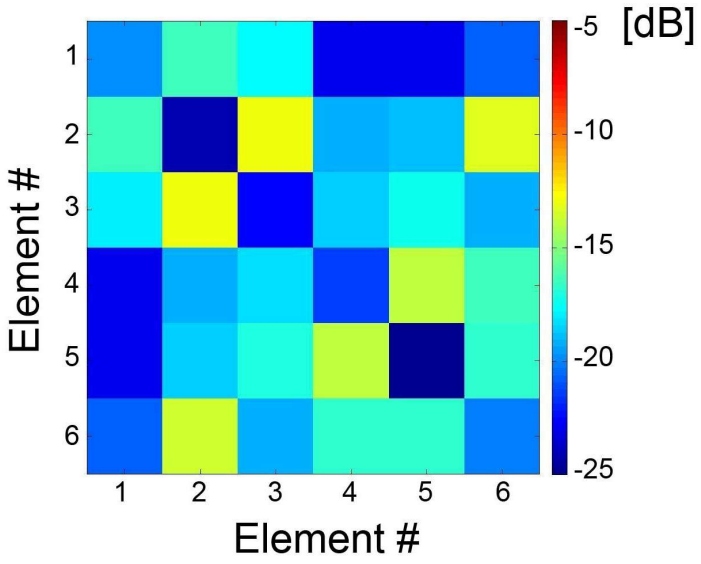

Figure 4: S-Parameter matrix averaged over 9 volunteers. Averaged values for reflection coefficients were found to be: -19.8 dB for S_{11}, -24.2 dB for S_{22}, -22.5 dB for S_{33}, -21.5 dB for S_{44}, -25.0 dB for S_{55}, -20.1 dB for S_{66}. The highest coupling occurs between elements 2/6 and between loop-elements which were capacitively decoupled: 2/3 and 4/5.

Electromagnetic Field and Specific Absorption Rate Simulations

The method used for B_1^+ optimization yielded more than one satisfactory solution. We chose the one that provided the highest B_1^+ homogeneity within the extended mask, here called the phase-optimized setting (PO). The algorithm provided phases for PO as follows: channel 1: 0°, channel 2: -202°, channel 3: -186°, channel 4: -282°, channel 5: -246°, channel 6: -279°. The B_1^+ homogeneity for PO was assessed in the defined volume of interest (VOI) which covered both eyes of the human voxel models, yielding a standard deviation: SD = 15.8 % for Ella and SD = 15.2 % for Duke (Figure 5).

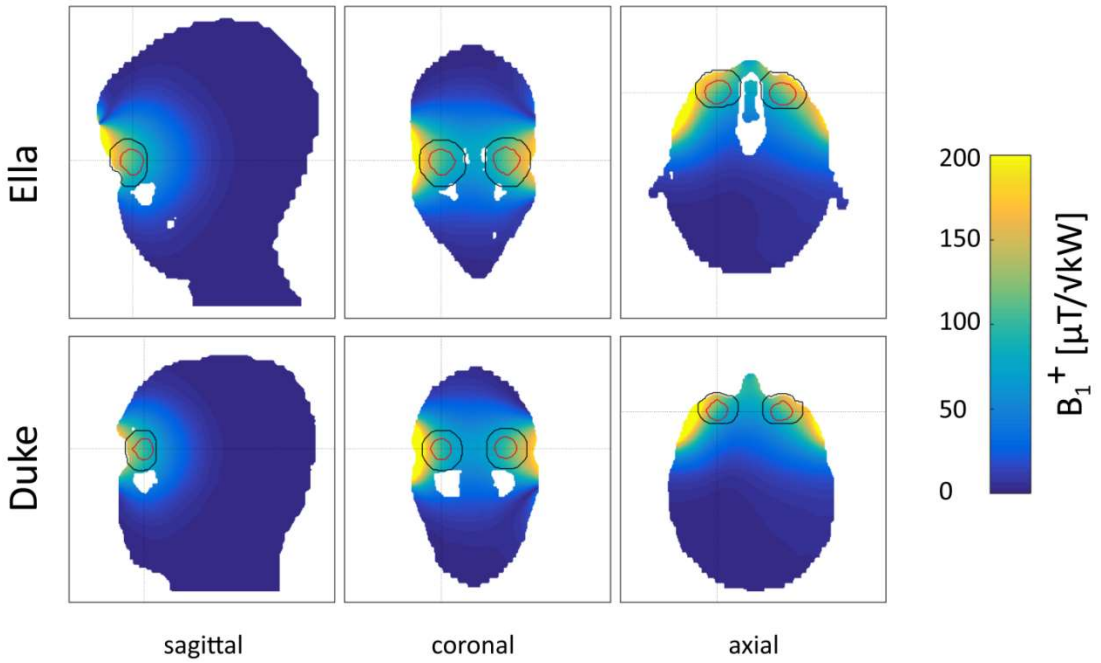

Figure 5: Transmit field (B_1^+) distribution for the phase-optimized setting (PO, channel 1: 0°, channel 2: -202°, channel 3: -186°, channel 4: -282°, channel 5: -246°, channel 6: -279°) in the sagittal, the coronal and the axial plane for human voxel models: Ella (top row) and Duke (bottom row). The red contours represent ROI covering the left and right eye which was used for estimation of B_1^+ homogeneity. It contains all tissues which are considered in the voxel model to belong to the eye: the vitreous humor, the sclera, the cornea and the lens. The black contours represent the extended mask which was provided an error margin and was used for the transmit field optimization.

Local SAR values averaged over 10 g (SAR_{10g}) were derived from the EMF simulations for PO using the human voxel models Duke and Ella (Figure 6) for an input power of 1 W. SAR simulations included the measured RF chain in order to accurately capture its losses and imperfections. Local SAR maxima were found to be 0.61 W/kg for Duke and 0.54 W/kg for Ella. Including a safety factor of 2.5, time-averaged forward power was limited to 6.7 W in order to stay below the 10 W/kg limit set by the IEC guidelines.

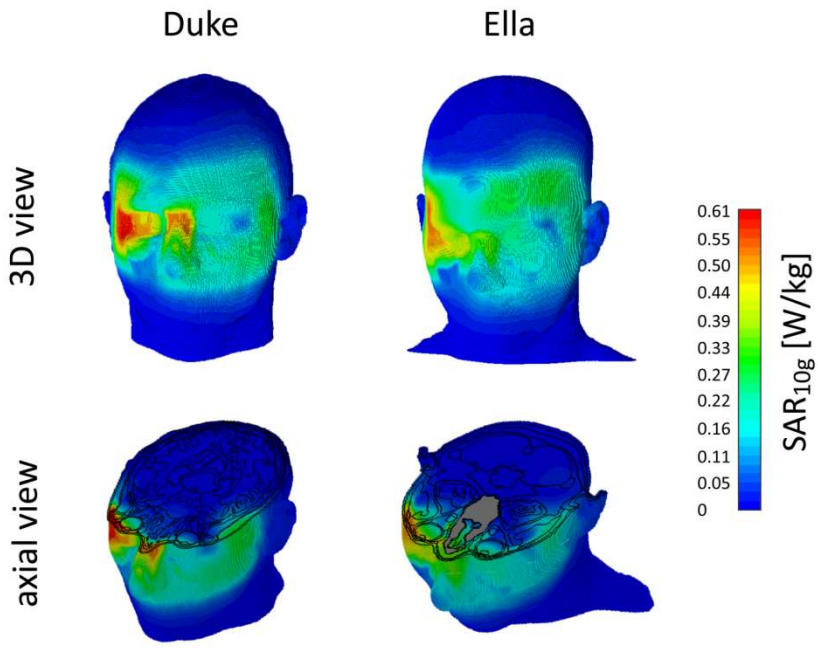

Figure 6: SAR_{10g} distribution for human voxel models Duke (left) and Ella (right) shown in 3D (top row) and for an axial view through the center of the eyes (bottom row). SAR_{10g} distributions were scaled to the maximum SAR_{10g} value for Duke (0.61 W/kg) in order to highlight good qualitative and quantitative (0.54 W/kg maximum SAR_{10g} value for Ella) agreement between SAR distributions for both human voxel models. The RF chain (its S-Matrix was measured by using a network analyzer) was included in the SAR simulations. Differences in SAR values arise from the anatomical differences between both models (mainly due to variations in shape of the skull and the nose).

Transmit Field Mapping

Phantom studies were conducted to compare the simulated B_1^+ distribution with the measured transmit field for PO which was later used for *in vivo* human imaging. A transversal slice through the center of the phantom was aligned with the center of the RF coil to determine whether there were differences between transmit field measurements and simulations (Figure 7A). The transmit field maps showed very good agreement both qualitatively and quantitatively (Figure 7B). These results demonstrate the validity of the RF coil design and support the credibility of the SAR simulations.

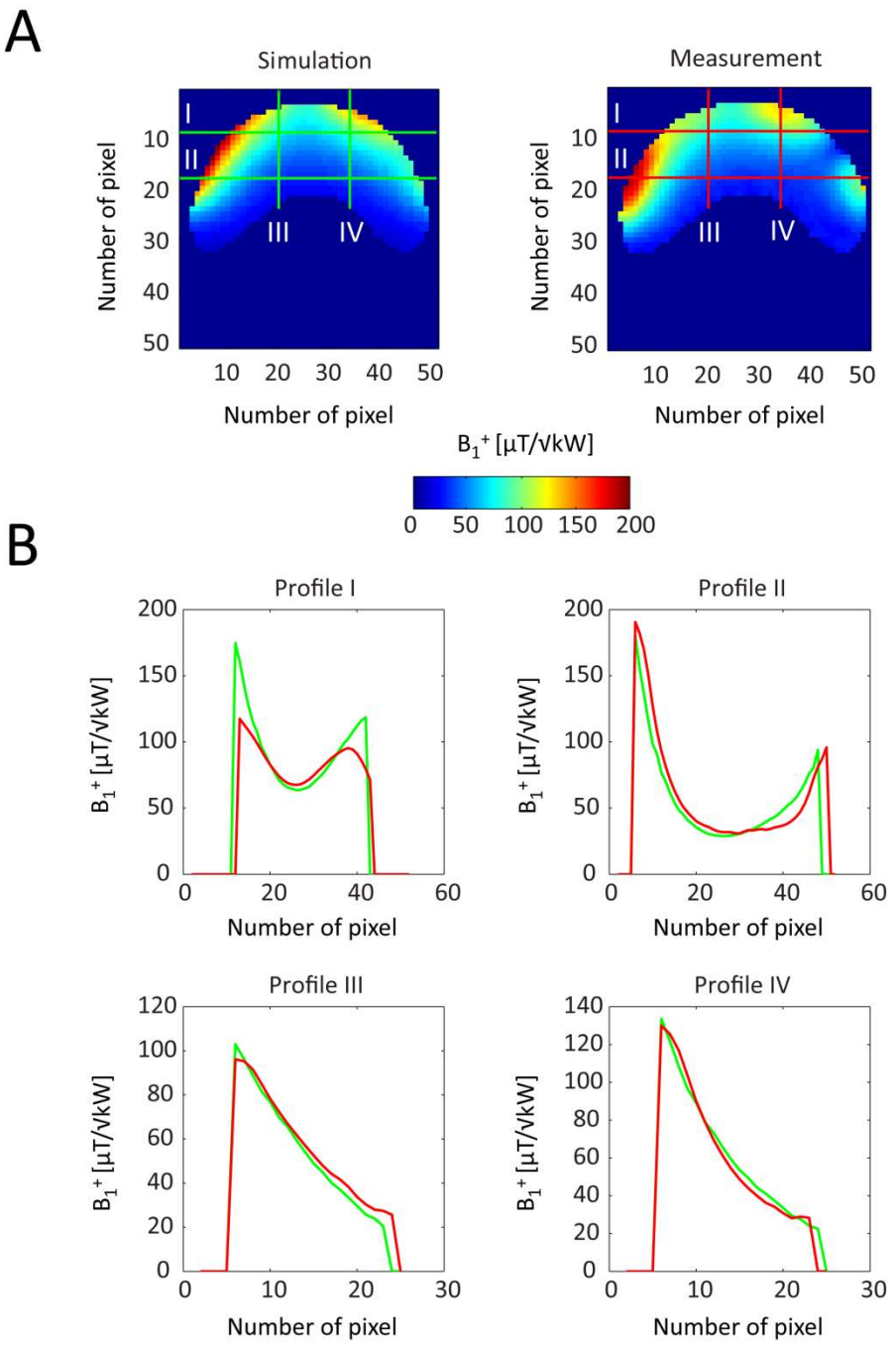

Figure 7: (A) Simulated (left) and measured (right) B_1^+ field distribution in a central axial slice of the cylindrical phantom. B_1^+ field was measured by using a phase-sensitive method. Two images with nominal flip angle FA = 90° were acquired: one with the non-selective composite pulse [$2\alpha_0$ α_{90}] and the other one with the first sub-pulse reversed in sign [$2\alpha_{180}$ α_{90}]. Pulse duration was 500 µs. The following parameters were used: TR= 160 ms, TE = 0.5 ms, number of projections = 15000, radial samples = 732, max gradient amplitude = 4 mT/m, max gradient slew rate = 170 mT/m/s, nominal isotropic resolution = 3.0 x 3.0 x 3.0 mm^3, pulse reference amplitude = 75 V. Flip angle maps were normalized to the RF input power. Four different profiles (I, II, III and IV) were drawn in both pictures. Light green color represents profiles for the simulated B_1^+ map and red color represents profiles for the measured B_1^+ map. (B) Quantitative comparison between all simulated and measured profiles. Simulated and measured data show very good agreement.

In vivo Feasibility Study

The *in vivo* feasibility study yielded high spatial resolution ^{23}Na MR images of the human eye at 7.0 T for female and male volunteers (Figure 8, 9 and 10). A nominal isotropic resolution of 1.4 mm^3 was achieved within an acquisition time (TA) of 10 minutes and 50 seconds. A nominal isotropic resolution of 1.0 mm^3 was achieved with TA = 14 minutes and 10 seconds. For the same spatial resolution, TA = 10 minutes and 50 seconds was used when TR was shortened to 13 ms. Three of the most important tissues in the context of sodium physiology can clearly be distinguished in all of the images: the vitreous humor, the aqueous humor and the lens.

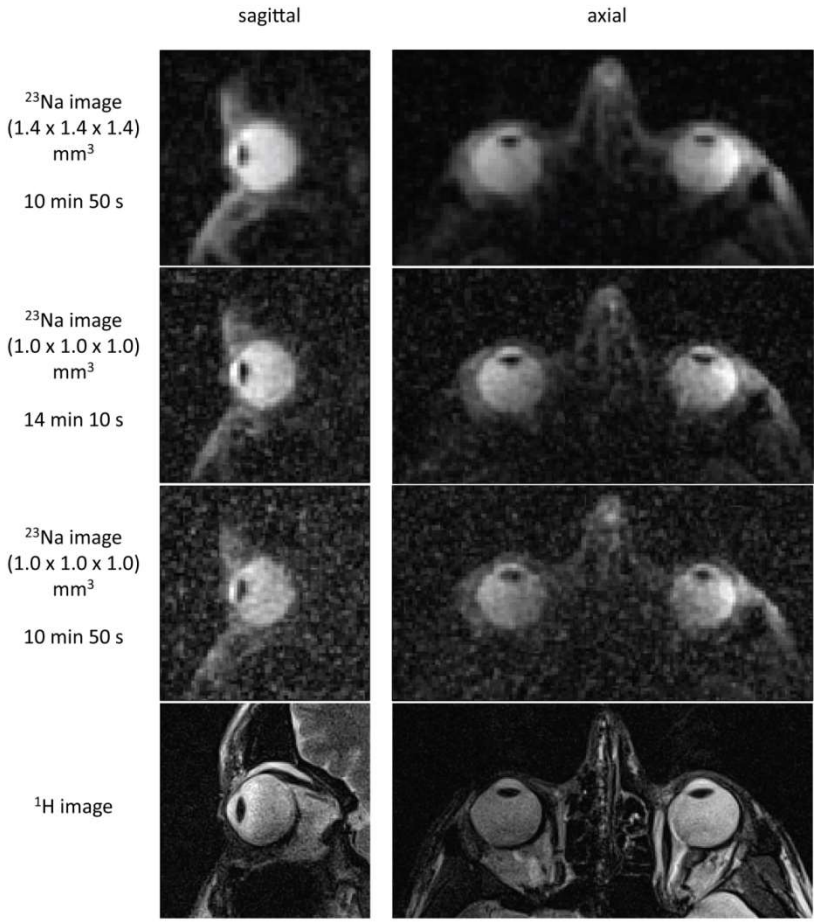

Figure 8: *In vivo* ^{23}Na image of the eyes of a healthy male volunteer (age = 26 years; BMI = 27.1 kg/m^2) obtained with DA-3DPR imaging and filtered with Hamming filter demonstrated in sagittal and axial view. No method for sensitivity correction was applied. First row: nominal isotropic resolution = 1.4 x 1.4 x 1.4 mm^3 was achieved within 10 minutes 50 seconds using following parameters: TR/TE = 13/0.55 ms, number of projections = 50000, readout duration = 9.2 ms. Second row: nominal isotropic resolution = 1.0 x 1.0 x 1.0 mm^3 was achieved within 14 minutes 10 seconds by using following parameters: TR/TE = 17/0.55 ms, number of projections = 50000, readout duration = 13.3 ms. Third row: nominal isotropic resolution = 1.0 x 1.0 x 1.0 mm^3 was achieved within 10 minutes 50 seconds by using following parameters: TR/TE = 13/0.55 ms, number of projections = 50000, readout duration = 9.3 ms.

Bottom row: proton reference images obtained with ^{1}H basic coil (Siemens, Erlangen, Germany) and T_2-weighted RARE imaging: TR/TE = 2940/74 ms, FOV = 384 x 384 mm^2, in-plane resolution = 0.54 x 0.54 mm^2, FA = 120°.

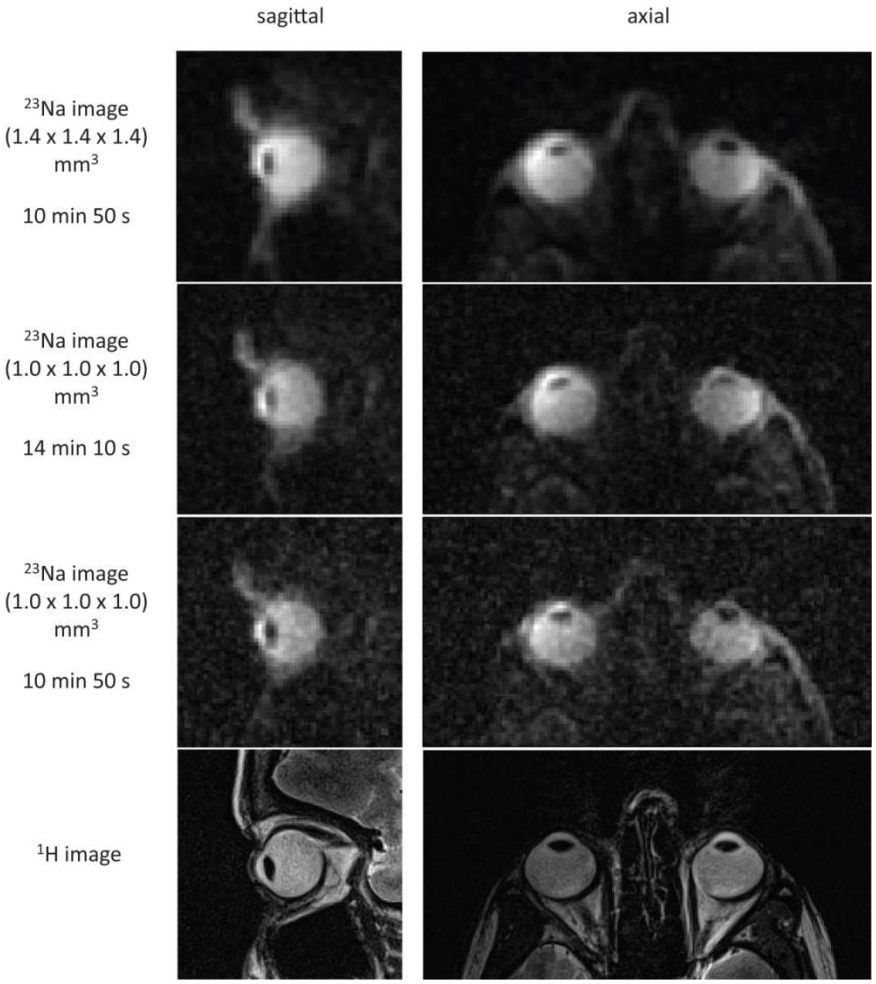

Figure 9: *In vivo* ^{23}Na image of the eyes of a healthy female volunteer (age = 29 years; BMI = 19.2 kg/m^2) obtained using the same pulse sequence parameters, imaging protocol and procedure as for the male volunteer shown in Figure 8.

SNR estimation of the data was conducted for one eye (sagittal slice in Fig. 7, 8 and 9) for female and male volunteers. The vitreous humor showed a mean $SNR_{male1} \approx 17$, mean $SNR_{male2} \approx 21$ and mean $SNR_{female} \approx 28$ for the data with isotropic resolution of 1.4 mm^3. A mean $SNR_{male1} \approx 7$, mean $SNR_{male2} \approx 8$ and mean $SNR_{female} \approx 12$ was observed for the data with isotropic resolution 1.0 mm^3 (TA = 10 min 50 sec). Aqueous humor yielded a mean $SNR_{male1} \approx 18$, mean $SNR_{male2} \approx 22$ and mean $SNR_{female} \approx 31$ for the acquisition using isotropic resolution of 1.4 mm^3. A mean $SNR_{male1} \approx 7$, mean $SNR_{male2} \approx 8$ and mean $SNR_{female} \approx 13$ was obtained for the images acquired with an isotropic resolution of 1.0 mm^3 (TA = 10 min 50 sec). The signal-to-noise ratio averaged over all subjects involved in this study showed a mean $SNR_{vitreous\ humor} = 20\pm4$ and mean $SNR_{aqueous\ humor} = 21\pm5$ for the spatial resolution of 1.4 mm

isotropic and mean $SNR_{vitreous\ humor}$ = 8±2 and mean $SNR_{aqueous\ humor}$ = 9±2 for the spatial resolution of 1.0 mm isotropic (TA = 10 min 50 sec). Images (central sagittal slice) obtained from female volunteers ($SNR_{vitreous\ humor}$ = 23±5 and mean $SNR_{aqueous\ humor}$ = 25±6) revealed higher SNR versus male volunteers ($SNR_{vitreous\ humor}$ = 17±2 and mean $SNR_{aqueous\ humor}$ = 18±2).

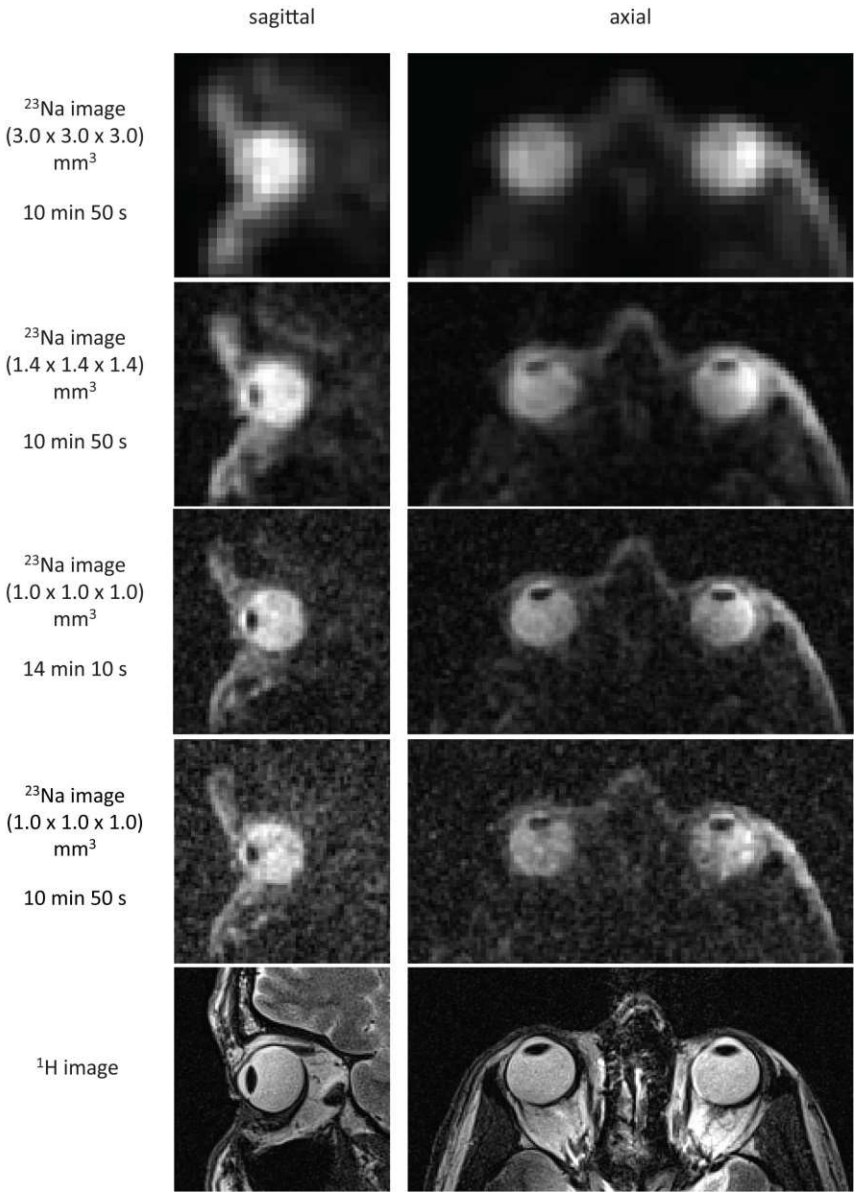

Figure 10: *In vivo* ^{23}Na image of the eyes of a healthy male volunteer (age = 53 years; BMI = 23.5 kg/m^2) obtained with an isotropic spatial resolution of 3 mm (top), 1.4 mm (middle) and 1.0 mm (bottom). A comparison between the low resolution data (3 mm isotropic) and the high resolution data (1.4 and 1.0 mm isotropic) facilitated by the performance gain of the proposed transceiver array underscores the need for enhanced spatial resolution to delineate all of the most important eye compartments.

Application of 3D-DLCS

^{23}Na MRI of the human eye was performed in one healthy, adult volunteer (sex: male; age = 26 years; BMI = 19.9 kg/m^2). The data acquired with $N_{projections}$ = 50000, $N_{averages}$ = 1, TA = 14.2 min were reconstructed with conventional gridding and applying Hamming filter (Figure 11). The data with $N_{projections}$ = 10000, $N_{averages}$ = 5, TA = 14.2 min were additionally reconstructed with the 3D-DLCS algorithm (block size B = 6, dictionary size D = 500, weighting parameter for dictionary representation λ = 0.5, sample number N_{samp} = 500000). Furthermore, one reconstruction was performed for a reduced dataset ($N_{averages}$ = 4, TA = 11.3 min). For sodium MRI of the eye two protocols were applied to achieve a nominal isotropic spatial resolution of 1 mm^3 within an identical total acquisition time (TA) of 14 min 10 s: (A) $N_{averages}$ = 1, $N_{projections}$ = 50000; (B) $N_{averages}$ = 5, $N_{projections}$ = 10000.

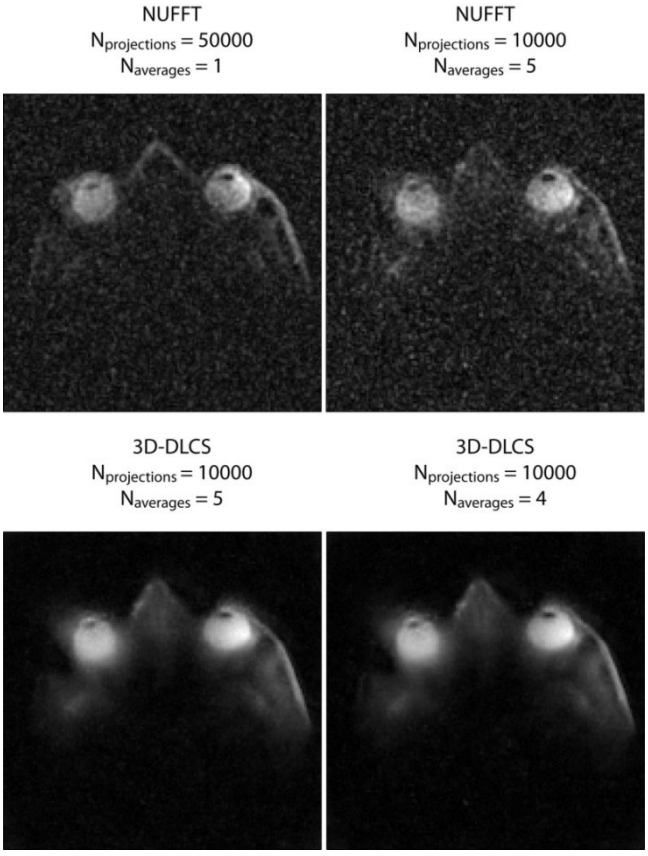

Figure 11: Comparison of images which resulted from using two different protocols: (A) $N_{averages}$ = 1, $N_{projections}$ = 50000 and (B) $N_{averages}$ = 5, $N_{projections}$ = 10000. Images were reconstructed with non-uniform fast Fourier transform (NUFFT) (top row) and with 3D dictionary learning compressed sensing (3D-DLCS) algorithm (bottom row). The image in bottom row (right) was obtained using only 4 averages what can be used in order to decrease scan time by about 3 minutes without losing fine details which are still present in the image.

Both datasets (A) and (B) were reconstructed with a standard reconstruction method and were used as baseline images. Dataset (B) was reconstructed with 3D dictionary learning compressed sensing (3D-DLCS) algorithm using 4 and 5 averages (Figure 11). Using only 4 averages instead of 5 does not lead to any drop in the performance of the 3D-DLCS reconstruction algorithm and the quality of the final image. This gain can be used to reduce total acquisition time for protocol (B) by almost 3 minutes. It is demonstrated that applying 3D ^{23}Na dictionary learning compressed sensing reconstruction for ^{23}Na *in vivo* MRI of the human eye at 7.0 Tesla preserves all of the details and leads to markedly reduced noise.

In Vivo Potassium (^{39}K) Magnetic Resonance Imaging of the Human Heart

Partial results of the work, which are presented in this chapter, have been published in:

D. Wenz, A.M. Nagel, J. Lott, A. Kuehne, S.C. Niesporek, T. Niendorf, „In Vivo Potassium MRI of the Human Heart at 7.0 Tesla“, *Magnetic Resonance in Medicine* 2019 Aug 27. doi: 10.1002/mrm.27951. [Epub ahead of print].

Radio Frequency Coil Design

The proposed RF coil design is comprised of two separate coil sets operating at f_{39K} = 13.9 MHz and f_{1H} = 297.2 MHz (Figure 12A,B). It consists of an anterior and a posterior module, the former curved to conform to human torso. Each module is composed of one large loop element (270x280mm^2) tuned to $f_{39K,}$ and two concentric smaller loop elements (220x200mm^2) tuned to f_{1H}. The ^{39}K loop elements are built of copper tube (outer diameter = 4 mm, wall thickness = 1 mm) and connected as a Helmholtz coil. The four ^{1}H loop elements (conductor width = 10 mm) were manufactured from 36 µm copper on a 0.5 mm FR-4 substrate. Constructive interference in the heart was achieved via static transmit field (B_1^+) shimming using appropriate phase delay cables. The adjacent ^{1}H loop elements share a common conductor and were decoupled capacitively using a trimmer capacitor. Each channel of the four-channel ^{1}H array was equipped with two cable traps tuned to f_{1H} and f_{39K}. For the ^{39}K Helmholtz coil, one cable trap tuned to f_{1H}, was used ($\lambda_{39K} \approx 22$ m). The size of the ^{39}K loop elements was chosen to provide acceptable signal uniformity in the ROI, and sufficient coverage of the heart. This latter criterion was also an important design consideration for the ^{1}H array, although its size was further modified to reduce coupling with the ^{39}K coil. No additional circuits were used to decouple ^{1}H from ^{39}K, as both resonance frequencies are sufficiently far away from each other (Figure 12C). The placement of the proposed ^{39}K/^{1}H RF coil is slightly off the long axis of the torso, which helps to keep the connection between Helmholtz loops as short as possible. The coil casing, shown in Figure 13, was designed by using Autodesk Inventor Professional 2017 (Autodesk Inc, San Rafael, CA) and constructed from ABS material using a 3D printer (BST 1200es; Dimension Inc, Eden Prairie, MN).

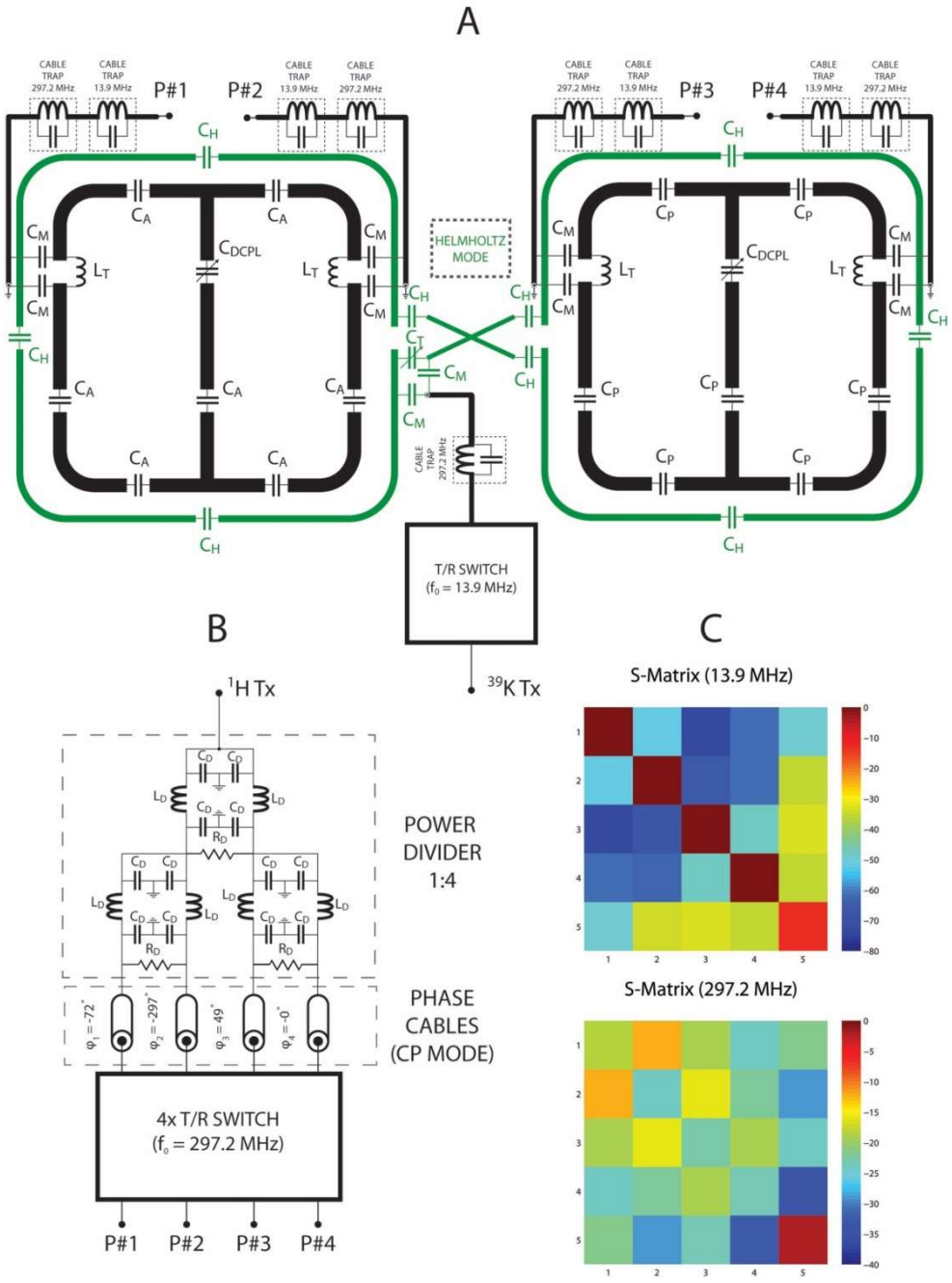

Figure 12: (A) Schematic of the proposed $^{39}K/^{1}H$ RF coil. The pair of ^{39}K Helmholtz loops are highlighted in green. Each loop is split equally by five capacitors C_H. The whole structure was tuned to the resonant frequency of 13.8 MHz and matched to 50 Ω using a balanced configuration. It is also equipped with one cable trap tuned to the resonant frequency of ^{1}H. The ^{39}K coil is connected through one T/R switch to the MR system. The four-channel ^{1}H transceiver array is in black. It was equally split with capacitors C_A (anterior part) and C_P (posterior part). The adjacent elements were decoupled using capacitor C_{DCPL}. Each of the elements was tuned to the resonant frequency of 297.2 MHz and matched to 50 Ω using a balanced configuration. Each channel was equipped with two cable traps tuned both resonant frequencies. (B) The RF signal was divided by using Wilkinson splitter and connected to the T/R switch box through phase cables which supported CP mode. (C) S-Parameter matrix averaged over 8 volunteers is shown for both resonant frequencies (13.9 and 297.2 MHz). Coupling between both coils was weaker at the lower frequency (S_{15} = -49.5 dB, S_{25}= -34.6 dB, S_{35}= -33.4 dB, S_{45}= -35.3 dB) than at the higher frequency (S_{15} = -21.8 dB, S_{25}= -29.3 dB, S_{35}= -23.4 dB, S_{45}= -33.0 dB). Averaged values for reflection coefficients

(297.2 MHz) were: -18.2 dB for S_{11}, -24.2 dB for S_{22}, -22.8 dB for S_{33}, -23.7 dB for S_{44}. The capacitive decoupling for the anterior part of the RF coil yielded S_{12} = -12.5 dB, and S_{23} = 16.0 dB for the posterior part.

Radio Frequency Coil Performance

The S-Matrices were measured at both resonance frequencies and averaged over 8 volunteers (Figure 12C). Prior to all measurements, the proposed RF coil was placed on the cylindrical phantom and tuned and matched. The average reflection coefficient S_{55} for the ^{39}K coil was -13.5 dB. Coupling between the ^{39}K coil and the four-channel ^{1}H array was found to be negligible at 13.9 MHz (all below -33.4 dB). Coupling at 297 MHz was within an acceptable range, between -21.8 dB and -33.0 dB. The phantom measurements yielded Q_{UL} = 141, Q_L = 27, and the Q_{UL}/Q_L = 5.2 for the ^{39}K Helmholtz coil.

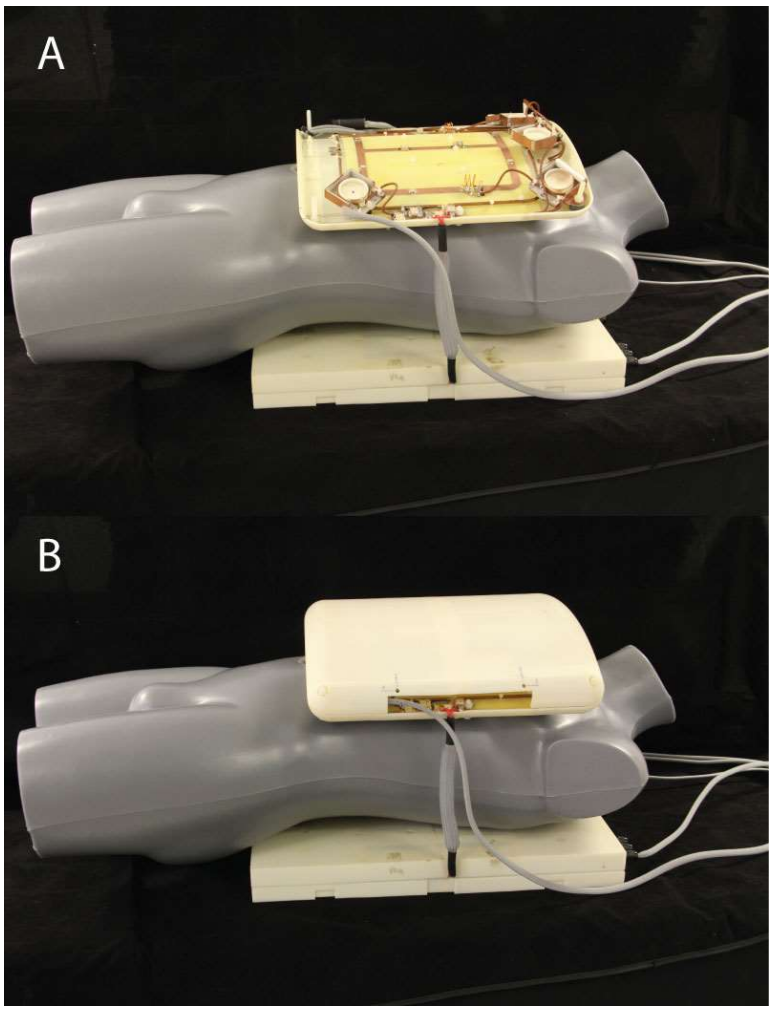

Figure 13: The proposed ^{39}K/^{1}H RF coil placed on a mannequin without (A) and with (B) upper part of the casing.

Electromagnetic Field and Specific Absorption Rate Simulations

To achieve the circularly polarized (CP) mode within the ROI in the human voxel model Duke, the phases were set to: channel 1: -72°, channel 2: -297°, channel 3: -49°, channel 4: 0°. The same phase setting was applied for the human voxel Ella (Figure 14). The B_1^+ distribution for ^{39}K was very similar for both human voxel models. The results for ^{1}H show that, despite obvious anatomical differences, the CP mode can be used to produce acceptable *in vivo* anatomical reference images.

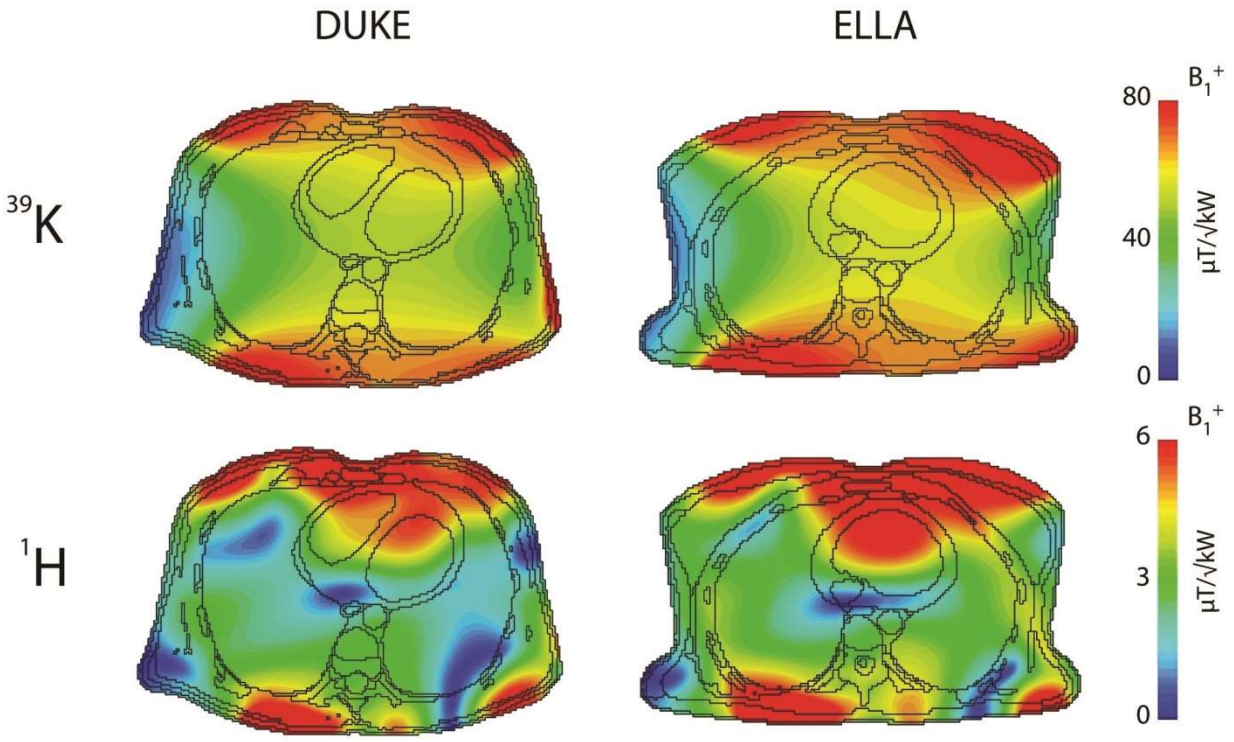

Figure 14: Transmit field (B_1^+) distribution for an axial cardiac plane of the human voxel models Duke (left) and Ella (right), for the resonant frequencies: 13.9 MHz (^{39}K, top row) and 297.2 MHz (^{1}H, bottom row). The black contours represent the anatomic features including the heart which is localized off-center. Based on qualitative assessment, the ^{39}K Helmholtz loops provide good B_1^+ homogeneity. The CP mode applied for the four-channel ^{1}H array provides fairly constructive B_1^+ interference for whole heart coverage.

Local SAR values averaged over 10 g (SAR_{10g}) were derived from the EMF simulations for both frequencies using the human voxel models Duke and Ella for an input power of 1 W (Figure 15). Local SAR maxima were found to be 0.21 W/kg for Duke and 0.23 W/kg for Ella for f_{39K} and 0.46 W/kg for Duke and 0.37 W/kg for Ella for f_{1H}. The ^{39}K RF coil was driven with time-averaged forward power limited to 100 W in order to stay below the 20 W/kg limit (first

level controlled SAR) set by the IEC guidelines. The time-averaged forward power for ^{1}H four-channel array was limited to 40 W.

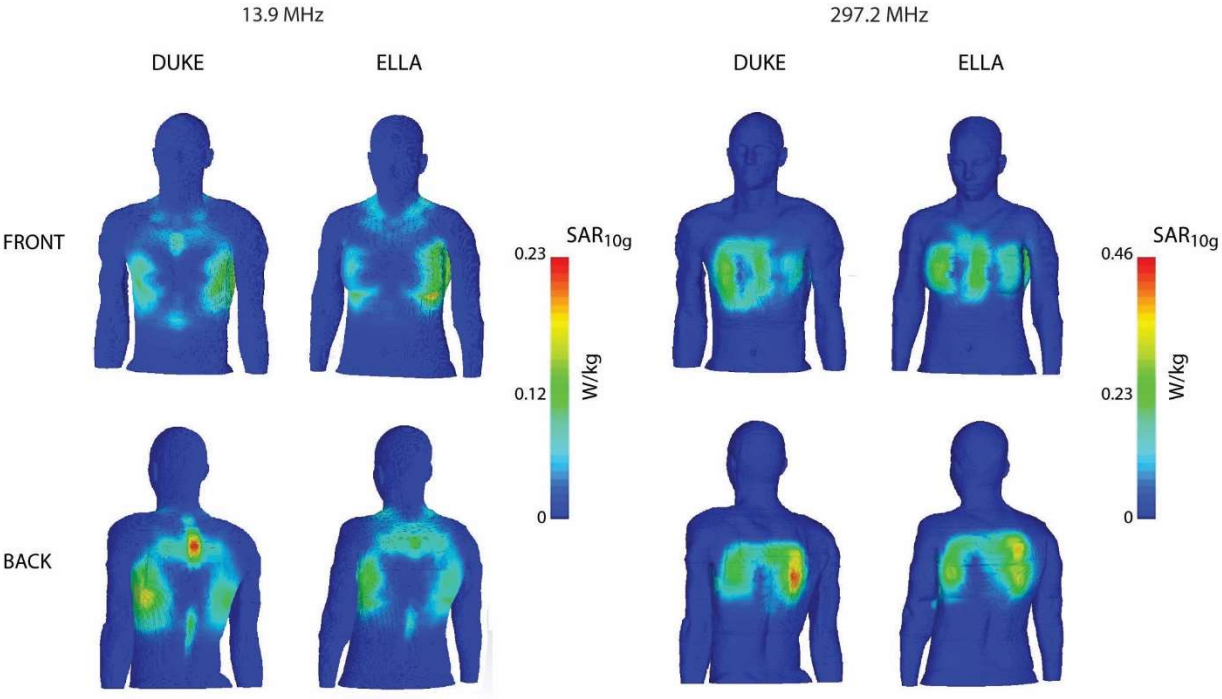

Figure 15: SAR_{10g} distribution for both resonant frequencies (13.9 and 297.2 MHz) for both human voxel models Duke and Ella shown in 3D. SAR_{10g} distributions were scaled to the maximum SAR_{10g} value for Ella (0.23 W/kg at 13.9 MHz) in order to highlight good qualitative and quantitative (0.21 W/kg maximum SAR_{10g} value for Duke) agreement between SAR distributions for both human voxel models. The maximum SAR_{10g} values obtained at 297.2 MHz were scaled to the maximum SAR_{10g} for Duke (0.46 W/kg at 297.2 MHz) which was slightly higher than for Ella (0.37 W/kg). A hotspot on the back of Duke at 13.9 MHz results from close vicinity of vertebral disc with respect to the conductive element of the RF coil. In case of Ella, the vertebral disc is located further away from the coil.

In Vivo Feasibility Study

The *in vivo* feasibility study which yielded ^{39}K images along with ^{1}H images of the human heart (Figure 16). For ^{39}K MRI of the heart, a nominal isotropic spatial resolution of (14.5x14.5x14.5) mm^3 was achieved within 30 minutes of scan time.

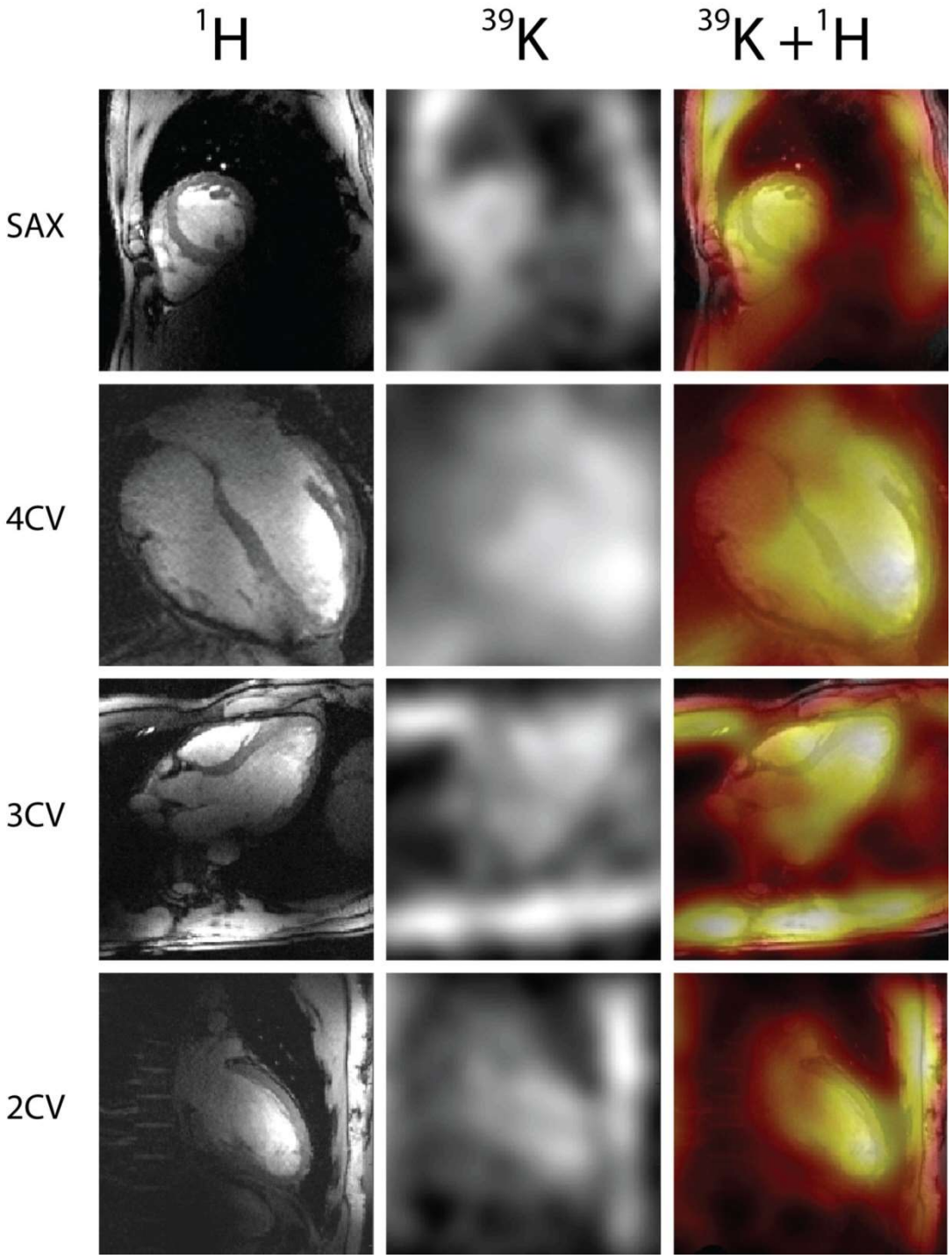

Figure 16: Left column: ^{1}H images of the heart obtained from a healthy male volunteer (age = 27 years; BMI = 27.1 kg/m^2) by using following parameters: TE/TR = 2.67/5.66 ms, FOV = (360 x 291) mm^2, in-plane resolution = (1.4 x 1.4) mm^2, slice thickness = 4.0 mm, flip angle = 32°, acquisition time = 12 s. Middle column: *in vivo* ^{39}K images of the same volunteer obtained using DA-3DPR imaging; filtered with Hamming filter and four-time zero filling and demonstrated in short axis (SAX), four-chamber (4CV), three-chamber (3CV) and two-chamber (2CV) view. The images were acquired with nominal isotropic resolution = 14.5 x 14.5 x 14.5 mm^3 within 30 minutes by using following parameters: TR/TE = 30/0.7 ms, number of projections = 20000, readout duration = 5 ms. Right column: overlay of ^{39}K and ^{1}H images.

The SNR within the heart was estimated by dividing the signal in the ROI by the standard deviation of the signal in the background. The average SNR (mean/SD) was SNR = 9.6 ± 2.4 (Figure 17; for male volunteers: MV1 = 9.2, MV2 = 8.7, MV3 = 8.7, MV4 = 6.3; for female volunteers: FV1 = 13.1, FV2 = 11.6). Based on supportive information obtained from anatomical reference images and the data that can be found in the literature (5,13), these regions correspond to the heart and the muscles of the thorax (anterior and posterior part). No significant destructive B_1^+ interferences were observed for the cardiac area used for ^{1}H MR.

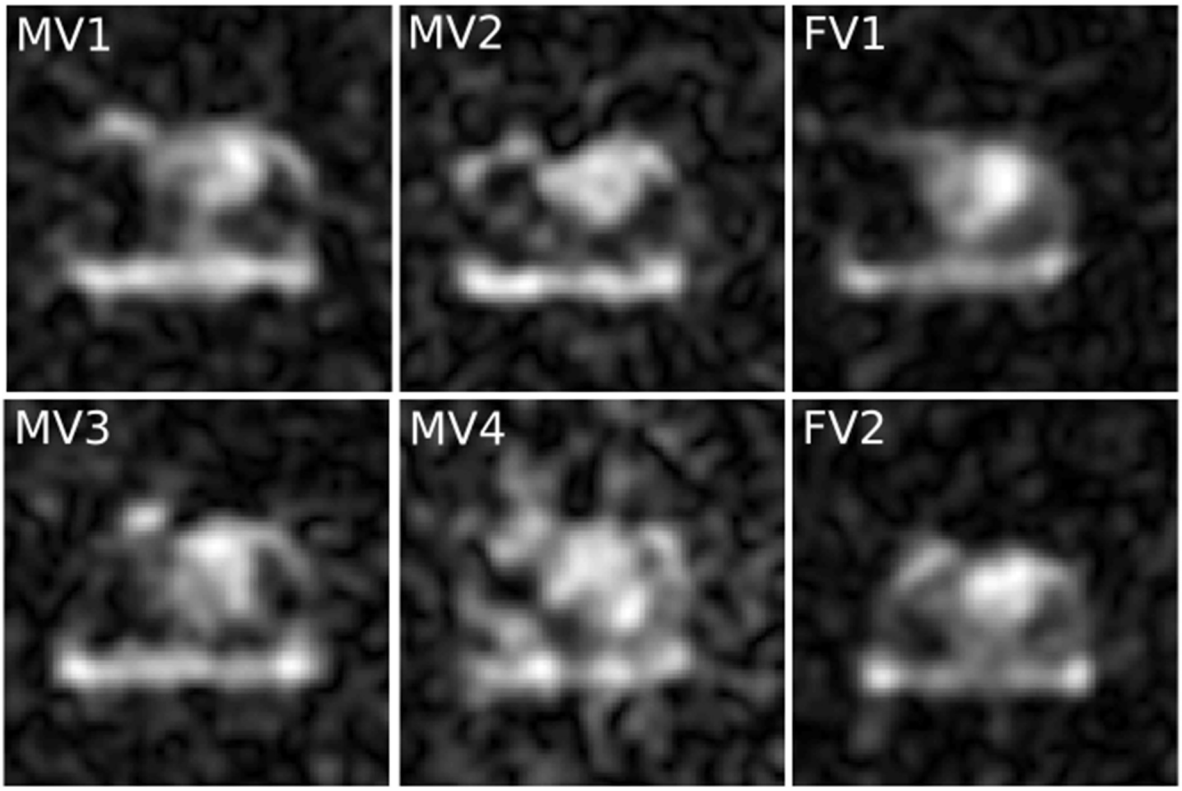

Figure 17. *In vivo* ^{39}K MR images, shown in axial view, obtained from six healthy volunteers: four male (MV1, MV2, MV3, MV4) and two female (FV1, FV2), using the same imaging technique as in Figure 16, but different MR system (Terra, Siemens Healthineers, Erlangen, Germany).

Discussion

Design of technology for ^{23}Na MRI of human eye

The first accomplishment of this work is to demonstrate that the proposed six-channel transceiver array supports high-spatial resolution, *in vivo* sodium imaging of the human eye at 7.0 T. Images were achieved with a nominal isotropic resolution of 1.4 mm^3 and 1.0 mm^3 within a clinically acceptable scan time of about 10 minutes. The quality of the images permits clear distinctions between the vitreous humor, the aqueous humor and the lens.

The data obtained for all of the receive channels were combined using the sum of squares method so that some of the lateral regions of the eyes appear brighter. To confirm the enhancement in spatial resolution permitted by the proposed transceiver array, data were acquired for healthy volunteers using exactly the same pulse sequence parameters and imaging protocol as for the 1.4 mm^3 spatial resolution scan, with the exception that the spatial resolution was set to 3.0 mm^3. The latter mimics the “typical” spatial resolution accomplished with volume coils tailored for ^{23}Na MRI of the brain [30]. Figure 10 surveys the data obtained with an isotropic spatial resolution of 3.0 mm, 1.4 mm and 1.0 mm and underscores the gain in spatial resolution performance achieved by the proposed transceiver array.

A second finding was that the 3D-DLCS reconstruction algorithm might be used for enhancing SNR in ^{23}Na *in vivo* MRI of the human eye. This gain can be used to reduce the total acquisition time or enhance the spatial resolution of images. Conceptually, this improvement makes even submillimeter ^{23}Na MRI of the human eye at 7.0 Tesla feasible within acceptable scan times.

The RF coil is light-weight and can be applied to a human head of average size and proportions. Our measurements reveal an acceptable level of sensitivity to different loading conditions that should not be an issue when used with patients. B_1^+ optimization yielded a phase setting with ample B_1^+ homogeneity within both eyes and low SAR values for both human voxel models Duke and Ella. Measured and simulated transmit field maps showed very good agreement. The proposed RF coil fulfills the safety requirements for local transmit arrays and poses no obstacles for future patient studies.

One issue relevant to this design that does not affect the validity of the findings should be noted as an area for further improvement. The author used inductive decoupling to reduce severe coupling between non-adjacent elements, but this is a costly solution. The issue affects both the transmit efficiency and SNR and becomes apparent when the Q_{UL}/Q_L ratio is analyzed for all the elements. As expected, the ratios are lowest for elements 3 and 6, which are

overloaded with inductors. At lower frequencies, RF coils do not couple as strongly to the load – a reason we expected the Q_{UL}/Q_L ratio to be worse than that found, for example, at 300 MHz (the resonant frequency of protons at 7.0 T). These losses should be considered in the development of new designs. One obvious solution would be to use a multi-channel receive-only array, which would probably provide benefits in terms of SNR, but this would require the design of a transmit-only (or transceiver) volume or semi-volume coil.

Clinical potential for imaging sodium in the eye

The potential of this project for clinical applications derives from the role of sodium in eye physiology. This discussion will consider the vitreous humor (VH), aqueous humor (AH) and the lens – tissues which are particularly clear in our images – as well as the retina, due to its key role in processing optical signals.

The concentration of Na^+ in the vitreous should be close to that of plasma, at around 135 mmol/l [31]. Changes in concentrations of substances in the vitreous body likely reflect processes in adjoining tissues.

Active secretion accounts for 80-90% of the total AH formation and is driven by primary active transport of Na^+ [32]. This triggers the movement of other molecules through cell membranes. The functions of other co-transporters such as Na^+/H^+ and Na-K-2Cl, which are involved in further processes, depend on Na^+ as well. This emphasizes the importance that Na^+ plays in AH formation and potential reabsorption.

Na^+ is also essential for the normal functioning of the retina. Retina cells produce large §amounts of water and accumulate lactic acid, which is toxic. The retinal pigment epithelium (RPE), is a layer of this structure located between the photoreceptor layer and blood-retina barrier and is responsible for the elimination of these substances [33]. The elimination of water is driven by Na^+/K^+-ATPase located in the RPE epithelium. Lactic acid is removed by the monocarboxylate transporter, which is driven by the activity of Na^+/H^+ exchanger.

The sodium concentration in the lens is much lower than in the VH, reported to be around 20 mmol/l. Ion circulation between the lens and the VH provides nutrients for the lens. This concentration gradient is driven by the activity of Na^+/K^+-ATPase, located in the lens epithelium [34].

The crucial nature of these processes involving sodium ions, as well as their roles in tissue homeostasis, suggest that various pathologies may lead to abnormal sodium concentrations in the fluid compartments and tissues of the eye. Since these changes are potentially detectable in MRI, it is quite plausible that a non-invasive method of measuring

sodium concentrations in patients with various eye disorders will contribute to our understanding of disease pathologies and also yield important new diagnostic information. A consideration of what is known about glaucoma and cataracts, which are the leading causes of blindness, as well as eye tumors yield some indication of the role of sodium and the potential changes it undergoes during the development of these diseases.

The biomedical literature contains multiple reports of elevated sodium content in different types of tumors [35-37]. Sodium imaging of the human eye *in vivo* at 7.0 T could be used as a complement to proton imaging data that might help in the planning of radiation treatments. Another potential use would be as a follow-up to proton beam therapy for intraocular tumors.

Glaucoma is often associated with higher intraocular pressure (IOP). Cole [11] found that reducing plasma sodium concentration, and thereby plasma osmolarity, led to a decrease in concentrations of sodium in the AH and an increase in IOP which lasted for several hours.

The characteristics of cataracts also suggest that sodium levels might be informative. Sodium ions play a very important role in the maintenance of the Na^+/K^+ gradient between the lens and vitreous humor. This gradient is regulated by Na^+/K^+-ATPase in the epithelial cell layer of the lens. Substances which change membrane permeability are likely to be cataractogenic. Ex vivo studies have reported elevated sodium concentrations in cataractous lenses [10].

The results support the statement that sodium content in the lens is distinguishable from sodium content in the aqueous and vitreous humor. The pathologic alterations discussed above reveal that these observations might have clinical importance in a number of contexts. The broad roles of this element in processes related to eye physiology suggest a range of questions for ophthalmological investigations.

Design of technology for ^{39}K MRI of human heart

The second accomplishment of this thesis is to demonstrate for the first time the feasibility of *in vivo* ^{39}K MRI of human heart at 7.0 T. *In vivo* experiments revealed three regions in the ^{39}K images with high signal intensity. Based on prior anatomical information, these correspond to the heart and thoracic muscles (anterior and posterior part). This is in agreement with the literature and previous studies which showed substantial K^+ content in muscle tissue [5]. The spatial resolution (14.5 mm^3 isotropic) and scan time (30 min) are encouraging for the development of clinical applications.

More than 20 years ago, Parrish et al. explored the theoretical basis for sodium and potassium MRI of the human heart at 1.5 T using simulations [12]. This pioneering work suggested that ^{39}K MRI of the heart with isotropic spatial resolution of 13 mm^3 and scan time of 30 minutes should be considered useful. These previous simulations revealed that the sensitivity that could be obtained at 1.5 T was not sufficient to achieve this goal, and that an 8-fold increase in SNR would be required. We were able to approach this threshold with our experiments at 7.0 T.

The proposed ^{39}K/^{1}H RF coil configuration supports *in vivo* ^{39}K and ^{1}H imaging of the human heart at 7.0 T. The ^{39}K/^{1}H RF coil is light-weight, ensures patient comfort and can be applied to an average human torso. Driving the ^{39}K loop elements in Helmholtz mode provides good B_1^+ field homogeneity, as demonstrated in our EMF simulations and in our *in vivo* measurements. The four-channel ^{1}H transceiver array yielded anatomical images of good quality to serve as a reference for the ^{39}K images.

In the proposed RF coil, the loop elements for both resonance frequencies are placed in close proximity to the target anatomy and ROI used for imaging. This is advantageous for transmit efficiency, and is particularly useful for receive sensitivity of imaging experiments involving ^{39}K ($\gamma_{1H}/\gamma_{39K} \cong 21$). An elliptical birdcage RF coil might serve as an alternative design, but to achieve a similar transmit efficiency as the proposed RF coil array, such a design would have to be a very close-fitting volume coil. The Q_{UL}/Q_L ratio of ^{39}K RF coil indicates that the losses are sample-dominated, which is not surprising for a large, close-fitting coil even at such a low resonant frequency.

Clinical potential of imaging potassium in the heart

Potassium ions are essential to survival, and their significance in cardiac physiology and metabolism extends beyond the function they play in the activity of Na^+/K^+-ATPase. Associations have been found between the K^+ channels expressed in human heart and higher risk of arrhythmias, but the molecular mechanisms that link them remain poorly understood [38]. New types of data should help expose the mechanisms that link changes in the expression and functioning of cardiac K^+ (and other) channels to arrhythmogenic cardiovascular disease.

Potassium is very important in regulation of smooth muscle tone and blood flow. Alteration in smooth muscle K^+ channel function may be involved in number of pathological conditions including vasospasm, hypertension, ischemia, hypotension during endotoxic shock and vascular reactivity during diabetes [14]. It has been demonstrated that irreversible injury

to myocytes is characterized by a decrease in tissue K^+. Researchers have also reported that the increase in extracellular K^+ concentrations caused by ischemia may underlie ventricular arrhythmia.

Pathological alterations in K^+ concentrations have profound clinical implications in a number of cardiovascular contexts, underscoring the broad roles of this element in processes related to heart physiology. *In vivo* ^{39}K MRI offers an interesting alternative in exploring tissue-specific pathophysiological changes, one which can complement ^{23}Na MRI-based techniques. The accuracy of methods currently used to distinguish between extracellular and intracellular sodium is a topic of considerable discussion. This makes ^{39}K MRI especially promising, since the physio-metabolic information it could provide can be associated almost exclusively with intracellular space.

Future directions

Another link between these two projects (eye and heart) lies in the growing realization that common mechanisms are engaged in cardiovascular disease and many eye diseases. This is particularly true with regard to aging and chronic conditions such as age-related macular degeneration, glaucoma and diabetic retinopathy [15]. In a sense this means that in the future, the eye might become a window into the heart. The eye is easily accessible and it is not only advantageous in the context of MRI, but also for other diagnostic devices developed for commercial purposes (e.g. initiative of Google), where the focus is to use the eye to predict cardiovascular risk.

It is important to realize that neither *in vivo* ^{23}Na nor *in vivo* ^{39}K MRI can provide SNR that would be comparable to standard anatomical ^{1}H imaging. The importance of these lies in the fact that they contribute to biomedical imaging in a different manner. Physio-metabolic parameters combined with biochemical dimensions such as concentration (volume or reaction) or reaction (millimoles/unit time) can be defined as “bioscales”. The unique possibility of quantification makes bioscales advantageous over biomarkers, which generally only correlate statistically to the outcome of a treatment [8].

Both of the proof-of-principle studies here are limited by the lack of quantification of Na^+ and K^+ concentrations. An accurate quantification of sodium content in the eye’s compartments or potassium content in the heart requires very well-validated algorithms. This might be solved by building two separate phantoms (one for ^{23}Na and the other one for ^{39}K) with proper T_1 and T_2 relaxation characteristics. Such phantoms would have to be designed in a way that the coupling between the RF coil and the phantom mimicked the interaction between the human

head/torso. Sodium/potassium content quantification also requires corrections for the B_0 field, transmit field and sensitivity. Another issue that needs to be addressed *en route* to reliable sodium quantification is correction for eye movement. This is of most relevance for the imaging of smaller compartments such as the aqueous humor and the lens. Since sodium *in vivo* imaging of the human eye has not yet been reported in patients, the author's knowledge is based on ex vivo studies. This makes it unclear what kind and magnitude of signal intensity or changes in sodium concentration might be characteristic of diseases and disorders of the eye under *in vivo* conditions. An important first step would be to carry out a qualitative study of these changes first in a small patient cohort as a mandatory precursor to broader patient studies involving the quantification of tissue sodium content.

The future of ^{23}Na and ^{39}K MRI of the heart will undoubtedly not end at 7.0 T, and the field is moving rapidly toward ultrahigh-field studies of such substances. Electrolyte mapping is a key application desired by the community of scientists and clinicians who are pushing for 14.0 T and 20.0 T human MR scanners [39], as outlined in a report of the National Research Council on high magnetic field science and its applications [40]. This report forwarded a call for a 20.0 Tesla wide-bore MR system – a technical development inspired by recent progress at 7.0 T. The sensitivity gain at 20.0 T is expected to reduce scan times e.g. for ^{39}K MRI by a factor of 8, compared to the 7.0 T capabilities available today. While this is, for the moment, merely a vision, it promises potassium MR with an isotropic spatial resolution of 8 mm (assuming linear noise model) achievable at a scan time comparable to that of our study. Together with other X-nuclei such as ^{23}Na and also ^{35}Cl, this will open new opportunities for ^{39}K MRI to drive the exploration of crucial structures, functions and physio-metabolic processes of the heart, eye and other tissues as a means of deepening our understanding of states of health and disease.

References

[1] Madelin G, Regatte RR. Biomedical applications of sodium MRI in vivo. J Magn Reson Imaging. 2013;38:511-529.

[2] Skou JC. The influence of some cations on an adenosine triphosphatase from peripheral nerves. Biochim Biophys Acta. 1957;23:394-401.

[3] Doyle DA, Morais Cabral J, Pfuetzner RA, Kuo A, Gulbis JM, Cohen SL, Chait BT, MacKinnon R. The structure of the potassium channel: molecular basis of K+ conduction and selectivity. Science. 1998;280:69-77.

[4] Cope FW, Damadian R. Cell potassium by 39K spin echo nuclear magnetic resonance. Nature. 1970;228:76-77.

[5] Umathum R, Rosler MB, Nagel AM. In vivo 39K MR imaging of human muscle and brain. Radiology. 2013;269:569-576.

[6] Rosler MB, Nagel AM, Umathum R, Bachert P, Benkhedah N. In vivo observation of quadrupolar splitting in (39)K magnetic resonance spectroscopy of human muscle tissue. NMR Biomed. 2016;29:451-457.

[7] Atkinson IC, Claiborne TC, Thulborn KR. Feasibility of 39-potassium MR imaging of a human brain at 9.4 Tesla. Magn Reson Med. 2014;71:1819-1825.

[8] Thulborn KR. Quantitative sodium MR imaging: A review of its evolving role in medicine. Neuroimage. 2018;168:250-268.

[9] Kolodny NH, Gragoudas ES, D'Amico DJ, Kohler SJ, Seddon JM, Murphy EJ, Yun C, Albert DM. Proton and sodium 23 magnetic resonance imaging of human ocular tissues. A model study. Arch Ophthalmol. 1987;105:1532-1536.

[10] Garner WH, Hilal SK, Lee SW, Spector A. Sodium-23 magnetic resonance imaging of the eye and lens. Proc Natl Acad Sci U S A. 1986;83:1901-1905.

[11] Cole DF. Some effects of decreased plasma sodium concentration on the composition and tension of the aqueous humour. Br J Ophthalmol. 1959;43:268-287.

[12] Parrish TB, Fieno DS, Fitzgerald SW, Judd RM. Theoretical basis for sodium and potassium MRI of the human heart at 1.5 T. Magn Reson Med. 1997;38:653-661.

[13]. Fieno DS, Kim RJ, Rehwald WG, Judd RM. Physiological basis for potassium (39K) magnetic resonance imaging of the heart. Circ Res. 1999;84:913-920.

[14] Nelson MT, Quayle JM. Physiological roles and properties of potassium channels in arterial smooth muscle. Am J Physiol. 1995;268:C799-822.

[15] Wong TY, Mitchell P. The eye in hypertension. Lancet. 2007;369:425-435.

[16] Roth GA, Johnson C, Abajobir A, Abd-Allah F, Abera SF, Abyu G, Ahmed M, Aksut B, Alam T, Alam K, Alla F, Alvis-Guzman N, Amrock S, Ansari H, Ärnlöv J, Asayesh H, Atey TM, Avila-Burgos L, Awasthi A, Banerjee A, Barac A, Bärnighausen T, Barregard L, Bedi N, Belay Ketema E, Bennett D, Berhe G, Bhutta Z, Bitew S, Carapetis J, Carrero JJ, Malta DC, Castañeda-Orjuela CA, Castillo-Rivas J, Catalá-López F, Choi JY, Christensen H, Cirillo M, Cooper L Jr, Criqui M, Cundiff D, Damasceno A, Dandona L, Dandona R, Davletov K, Dharmaratne S, Dorairaj P, Dubey M, Ehrenkranz R, El Sayed Zaki M, Faraon EJA, Esteghamati A, Farid T, Farvid M, Feigin V, Ding EL, Fowkes G, Gebrehiwot T, Gillum R, Gold A, Gona P, Gupta R, Habtewold TD, Hafezi-Nejad N, Hailu T, Hailu G, Hankey G, Hassen HY, Abate KH, Havmoeller R, Hay SI, Horino M, Hotez PJ, Jacobsen K, James S, Javanbakht M, Jeemon P, John D, Jonas J, Kalkonde Y, Karimkhani C, Kasaeian A, Khader Y, Khan A, Khang YH, Khera S, Khoja AT, Khubchandani J, Kim D, Kolte D, Kosen S, Krohn KJ, Kumar GA, Kwan GF, Lal DK, Larsson A, Linn S, Lopez A, Lotufo PA, El Razek HMA, Malekzadeh R, Mazidi M, Meier T, Meles KG, Mensah G, Meretoja A, Mezgebe H, Miller T, Mirrakhimov E, Mohammed S, Moran AE, Musa KI, Narula J, Neal B, Ngalesoni F, Nguyen G, Obermeyer CM, Owolabi M, Patton G, Pedro J, Qato D, Qorbani M, Rahimi K, Rai RK, Rawaf S, Ribeiro A, Safiri S, Salomon JA, Santos I, Santric Milicevic M, Sartorius B, Schutte A, Sepanlou S, Shaikh MA, Shin MJ, Shishehbor M, Shore H, Silva DAS, Sobngwi E, Stranges S, Swaminathan S, Tabarés-Seisdedos R, Tadele Atnafu N, Tesfay F, Thakur JS, Thrift A, Topor-Madry R, Truelsen T, Tyrovolas S, Ukwaja KN, Uthman O, Vasankari T, Vlassov V, Vollset SE, Wakayo T, Watkins D, Weintraub R, Werdecker A, Westerman R, Wiysonge CS, Wolfe C, Workicho A, Xu G, Yano Y, Yip P, Yonemoto N, Younis M, Yu C, Vos T, Naghavi M, Murray C. Global, Regional, and National Burden of Cardiovascular Diseases for 10 Causes, 1990 to 2015. J Am Coll Cardiol. 2017;70:1-25.

[17] Roemer PB, Edelstein WA, Hayes CE, Souza SP, Mueller OM. The NMR phased array. Magn Reson Med. 1990;16:192-225.

[18] Shen GX, Boada FE, Thulborn KR. Dual-frequency, dual-quadrature, birdcage RF coil design with identical B1 pattern for sodium and proton imaging of the human brain at 1.5 T. Magn Reson Med. 1997;38:717-725.

[19] Stobbe R, Beaulieu C. In vivo sodium magnetic resonance imaging of the human brain using soft inversion recovery fluid attenuation. Magn Reson Med. 2005;54:1305-1310.

[20] Qian Y, Zhao T, Wiggins GC, Wald LL, Zheng H, Weimer J, Boada FE. Sodium imaging of human brain at 7 T with 15-channel array coil. Magn Reson Med. 2012;68:1807-1814.

[21] Shajan G, Mirkes C, Buckenmaier K, Hoffmann J, Pohmann R, Scheffler K. Three-layered radio frequency coil arrangement for sodium MRI of the human brain at 9.4 Tesla. Magn Reson Med. 2016;75:906-916.

[22] Hasgall PA, Di Gennaro F, Baumgartner C, Neufeld E, Lloyd B, Gosselin MC, Payne D, Klingenboeck A, Kuster N. IT'IS Database for thermal and electromagnetic parameters of biological tissues. Version 4.0, May 15, 2018.

[23] Kuehne A, Goluch S, Waxmann P, Seifert F, Ittermann B, Moser E, Laistler E. Power balance and loss mechanism analysis in RF transmit coil arrays. Magn Reson Med. 2015;74:1165-1176.

[24] International Electrotechnical Commision. Medical electrical equipment. Part 2-33: Particular requirements for the safety of magnetic resonance equipment for medical diagnosis. Volume 60601-2-33 Ed.3. Geneva, Switzerland: International Electrotechnical Commission.

[25] Nagel AM, Laun FB, Weber MA, Matthies C, Semmler W, Schad LR. Sodium MRI using a density-adapted 3D radial acquisition technique. Magn Reson Med. 2009;62:1565-1573.

[26] Morrell GR. A phase-sensitive method of flip angle mapping. Magn Reson Med. 2008;60:889-894.

[27] Lustig M, Donoho D, Pauly JM. Sparse MRI: The application of compressed sensing for rapid MR imaging. Magn Reson Med. 2007;58:1182-1195.

[28] Behl NG, Gnahm C, Bachert P, Ladd ME, Nagel AM. Three-dimensional dictionary-learning reconstruction of (23)Na MRI data. Magn Reson Med. 2016;75:1605-1616.

[29] Kumar A, Edelstein WA, Bottomley PA. Noise figure limits for circular loop MR coils. Magn Reson Med. 2009;61:1201-1209.

[30] Nagel AM, Bock M, Hartmann C, Gerigk L, Neumann JO, Weber MA, Bendszus M, Radbruch A, Wick W, Schlemmer HP, Semmler W, Biller A. The potential of relaxation-weighted sodium magnetic resonance imaging as demonstrated on brain tumors. Invest Radiol. 2011;46:539-547.

[31] Kaufman PL, Adler FH, Levin LA, Alm A. Adler's Physiology of the Eye. Elsevier Health Sciences 2011.

[32] Avila MY, Seidler RW, Stone RA, Civan MM. Inhibitors of NHE-1 Na+/H+ exchange reduce mouse intraocular pressure. Invest Ophthalmol Vis Sci. 2002;43:1897-1902.

[33] Strauss O. The retinal pigment epithelium in visual function. Physiol Rev. 2005;85:845-881.

[34] Reddy VN. Transport of organic molecules in the lens. Exp Eye Res. 1973;15:731-750.

[35] Cameron IL, Smith NK, Pool TB, Sparks RL. Intracellular concentration of sodium and other elements as related to mitogenesis and oncogenesis in vivo. Cancer Res. 1980;40:1493-1500.

[36] Ouwerkerk R, Bleich KB, Gillen JS, Pomper MG, Bottomley PA. Tissue sodium concentration in human brain tumors as measured with 23Na MR imaging. Radiology. 2003;227:529-537.

[37] Ouwerkerk R, Jacobs MA, Macura KJ, Wolff AC, Stearns V, Mezban SD, Khouri NF, Bluemke DA, Bottomley PA. Elevated tissue sodium concentration in malignant breast lesions detected with non-invasive 23Na MRI. Breast Cancer Res Treat. 2007;106:151-160.

[38] Giudicessi JR, Ackerman MJ. Potassium-channel mutations and cardiac arrhythmias--diagnosis and therapy. Nat Rev Cardiol. 2012;9:319-332.

[39] Budinger TF, Bird MD. MRI and MRS of the human brain at magnetic fields of 14T to 20T: Technical feasibility, safety, and neuroscience horizons. Neuroimage. 2018;168:509-531.

[40] In: National Research Council High Magnetic Field Science and Its Application in the United States: Current Status and Future Directions. Washington, DC: The National Academies Press; 2013.

Eidesstattliche Versicherung

„Ich, Daniel Wenz, versichere an Eides statt durch meine eigenhändige Unterschrift, dass ich die vorgelegte Dissertation mit dem Thema: *Entwicklung der Multi-Kanal-Hochfrequenz Technologie für Natrium und Kalium Magnet-Resonanz-Tomographie bei 7.0 Tesla: Entwurf und klinische Anwendung/ Development of multi-channel radio frequency technology for sodium and potassium magnetic resonance imaging at 7.0 Tesla: design and clinical application* selbstständig und ohne nicht offengelegte Hilfe Dritter verfasst und keine anderen als die angegebenen Quellen und Hilfsmittel genutzt habe.

Alle Stellen, die wörtlich oder dem Sinne nach auf Publikationen oder Vorträgen anderer Autoren beruhen, sind als solche in korrekter Zitierung kenntlich gemacht. Die Abschnitte zu Methodik (insbesondere praktische Arbeiten, Laborbestimmungen, statistische Aufarbeitung) und Resultaten (insbesondere Abbildungen, Graphiken und Tabellen) werden von mir verantwortet.

Meine Anteile an etwaigen Publikationen zu dieser Dissertation entsprechen denen, die in der untenstehenden gemeinsamen Erklärung mit dem/der Erstbetreuer/in, angegeben sind. Für sämtliche im Rahmen der Dissertation entstandenen Publikationen wurden die Richtlinien des ICMJE (International Committee of Medical Journal Editors; www.icmje.og) zur Autorenschaft eingehalten. Ich erkläre ferner, dass mir die Satzung der Charité – Universitätsmedizin Berlin zur Sicherung Guter Wissenschaftlicher Praxis bekannt ist und ich mich zur Einhaltung dieser Satzung verpflichte.

Die Bedeutung dieser eidesstattlichen Versicherung und die strafrechtlichen Folgen einer unwahren eidesstattlichen Versicherung (§§156, 161 des Strafgesetzbuches) sind mir bekannt und bewusst.“

_____

Datum Unterschrift

Anteilserklärung an den erfolgten Publikationen

Daniel Wenz hatte folgenden Anteil an den folgenden Publikationen:

Publikation 1:

D. Wenz, A. Kuehne, T. Huelnhagen, A.M. Nagel, H. Waiczies, O. Weinberger, C. Oezerdem, O. Stachs, S. Langner, E. Seeliger, B. Flemming, R. Hodge, T. Niendorf, “Millimeter Spatial Resolution In Vivo Sodium MRI of the Human Eye at 7 T Using a Dedicated Radiofrequency Transceiver Array”, *Magnetic Resonance in Medicine* 2018 Aug;80(2):672-684. doi: 10.1002/mrm.27053.

Journal Impact Factor (ISI-Web-Liste 2016): 3,924

Journal Impact Factor (ISI-Web-Liste 2017): 4,082

Journal Impact Factor (ISI-Web-Liste 2018): 3,858

Daniel Wenz was responsible for the concept of the study and profound literature research. The literature research was particularly important in the context of finding potential clinical applications of in vivo sodium magnetic resonance imaging of the eye. Daniel Wenz designed the six-channel transmit/receive radio frequency coil array for sodium MRI of the human eye at 7.0 Tesla. He performed the radio frequency circuit simulations and the electromagnetic field simulations in phantoms and human voxel models. He conducted specific absorption rate simulations in human voxel models and defined radio frequency power limits for all of the experiments. Mr. Wenz built the six-channel transmit/receive radio frequency coil array, characterized and evaluated it at the bench. He optimized the radio frequency pulse sequence parameters in order to obtain the enhanced spatial resolution. He performed all of the phantom experiments, transmit field mapping and all in vivo experiments in humans. He was responsible for critical analysis and interpretation of the obtained data. He wrote the manuscript and was responsible for all of the revised versions of the manuscript. He prepared all of the figures, excluding Figure 4.

Publikation 2:

D. Wenz, A.M. Nagel, J. Lott, A. Kuehne, S.C. Niesporek, T. Niendorf, „In Vivo Potassium MRI of the Human Heart at 7.0 Tesla“, *Magnetic Resonance in Medicine* 2019 Aug 27. doi: 10.1002/mrm.27951. [Epub ahead of print]

Journal Impact Factor (ISI-Web-Liste 2016): 3,924

Journal Impact Factor (ISI-Web-Liste 2017): 4,082

Journal Impact Factor (ISI-Web-Liste 2018): 3,858

Daniel Wenz was responsible for the concept of the study and profound literature research. The literature research was particularly important in the context of finding potential clinical applications of potassium magnetic resonance imaging of the heart. Daniel Wenz designed the two/four-channel $^{39}K/^{1}H$ transmit/receive radio frequency coil for potassium/proton MRI of the human heart at 7.0 Tesla. He performed the radio frequency circuit simulations and the electromagnetic field simulations in phantoms and human voxel models. He conducted specific absorption rate simulations in human voxel models and provided the radio frequency power limits for all of the experiments. Mr. Wenz built the two/four-channel $^{39}K/^{1}H$ transmit/receive radio frequency coil, characterized and evaluated it at the bench. He performed all of the phantom experiments and all in vivo experiments in humans. He was responsible for critical analysis and interpretation of the obtained data. He wrote the manuscript and was responsible for all of the revised versions of the manuscript. He prepared all of the figures in the manuscript.

_____

Unterschrift, Datum und Stempel des/der erstbetreuenden Hochschullehrers/in

_____

Unterschrift des Doktoranden/der Doktorandin

Journal Data Filtered By: **Selected JCR Year: 2016** Selected Editions: SCIE,SSCI Selected Categories: **"RADIOLOGY, NUCLEAR MEDICINE and MEDICAL IMAGING"** Selected Category Scheme: WoS

Gesamtanzahl: 126 Journale

Rank	Full Journal Title	Total Cites	Journal Impact Factor	Eigenfactor Score
1	JACC-Cardiovascular Imaging	6,895	10.189	0.027050
2	RADIOLOGY	50,983	7.296	0.066140
3	EUROPEAN JOURNAL OF NUCLEAR MEDICINE AND MOLECULAR IMAGING	14,019	7.277	0.024910
4	Circulation-Cardiovascular Imaging	4,472	6.803	0.019120
5	JOURNAL OF NUCLEAR MEDICINE	24,977	6.646	0.037540
6	NEUROIMAGE	85,630	5.835	0.173210
7	JOURNAL OF CARDIOVASCULAR MAGNETIC RESONANCE	4,349	5.601	0.014950
8	SEMINARS IN RADIATION ONCOLOGY	2,232	5.356	0.003910
9	INVESTIGATIVE RADIOLOGY	5,925	5.195	0.011230
10	INTERNATIONAL JOURNAL OF RADIATION ONCOLOGY BIOLOGY PHYSICS	44,068	5.133	0.060060
11	ULTRASOUND IN OBSTETRICS & GYNECOLOGY	11,611	4.710	0.019350
12	HUMAN BRAIN MAPPING	18,139	4.530	0.041900
13	RADIOTHERAPY AND ONCOLOGY	15,639	4.328	0.028040
14	MEDICAL IMAGE ANALYSIS	5,539	4.188	0.010720
15	EUROPEAN RADIOLOGY	16,381	3.967	0.033340
16	IEEE TRANSACTIONS ON MEDICAL IMAGING	15,215	3.942	0.019660
17	JOURNAL OF NUCLEAR CARDIOLOGY	3,021	3.930	0.003920
18	MAGNETIC RESONANCE IN MEDICINE	29,816	3.924	0.035960
19	CLINICAL NUCLEAR MEDICINE	4,008	3.640	0.006470
20	SEMINARS IN NUCLEAR MEDICINE	2,056	3.630	0.002800
21	AMERICAN JOURNAL OF NEURORADIOLOGY	21,720	3.550	0.032180
22	MOLECULAR IMAGING AND BIOLOGY	2,228	3.466	0.005880
23	ULTRASCHALL IN DER MEDIZIN	1,907	3.452	0.003930
24	RADIOGRAPHICS	10,286	3.427	0.009660
25	Biomedical Optics Express	6,187	3.337	0.021610
26	Contrast Media & Molecular Imaging	1,131	3.307	0.002810
27	INTERNATIONAL JOURNAL OF HYPERTHERMIA	3,030	3.262	0.003810

Journal Data Filtered By: **Selected JCR Year: 2017** Selected Editions: SCIE,SSCI Selected Categories: **"RADIOLOGY, NUCLEAR MEDICINE and MEDICAL IMAGING"** Selected Category Scheme: WoS

Gesamtanzahl: 128 Journale

Rank	Full Journal Title	Total Cites	Journal Impact Factor	Eigenfactor Score
1	JACC-Cardiovascular Imaging	8,104	10.247	0.026360
2	European Heart Journal-Cardiovascular Imaging	4,630	8.336	0.020640
3	EUROPEAN JOURNAL OF NUCLEAR MEDICINE AND MOLECULAR IMAGING	14,983	7.704	0.024870
4	RADIOLOGY	54,109	7.469	0.063710
5	JOURNAL OF NUCLEAR MEDICINE	27,101	7.439	0.037560
6	CLINICAL NUCLEAR MEDICINE	4,756	6.281	0.006950
7	INVESTIGATIVE RADIOLOGY	6,486	6.224	0.012410
8	Circulation-Cardiovascular Imaging	5,438	6.221	0.020160
9	IEEE TRANSACTIONS ON MEDICAL IMAGING	17,837	6.131	0.024200
10	ULTRASOUND IN OBSTETRICS & GYNECOLOGY	12,420	5.654	0.018820
11	INTERNATIONAL JOURNAL OF RADIATION ONCOLOGY BIOLOGY PHYSICS	46,595	5.554	0.055060
12	JOURNAL OF CARDIOVASCULAR MAGNETIC RESONANCE	4,918	5.457	0.013530
13	NEUROIMAGE	92,719	5.426	0.152610
14	MEDICAL IMAGE ANALYSIS	6,383	5.356	0.011900
15	RADIOTHERAPY AND ONCOLOGY	17,184	4.942	0.027840
16	HUMAN BRAIN MAPPING	20,334	4.927	0.042810
17	SEMINARS IN NUCLEAR MEDICINE	2,285	4.558	0.002990
18	ULTRASCHALL IN DER MEDIZIN	2,201	4.389	0.004310
19	MAGNETIC RESONANCE IN MEDICINE	31,440	4.082	0.034130
20	EUROPEAN RADIOLOGY	18,615	4.027	0.034120
20	SEMINARS IN RADIATION ONCOLOGY	2,480	4.027	0.003620
22	JOURNAL OF NUCLEAR CARDIOLOGY	3,508	3.847	0.004120
23	AMERICAN JOURNAL OF NEURORADIOLOGY	22,667	3.653	0.029840
24	JOURNAL OF MAGNETIC RESONANCE IMAGING	16,398	3.612	0.027440
25	MOLECULAR IMAGING AND BIOLOGY	2,415	3.608	0.005480

Journal Data Filtered By: **Selected JCR Year: 2018** Selected Editions: SCIE,SSCI Selected Categories: **"RADIOLOGY, NUCLEAR MEDICINE and MEDICAL IMAGING"** Selected Category Scheme: WoS

Gesamtanzahl: 129 Journale

Rank	Full Journal Title	Total Cites	Journal Impact Factor	Eigenfactor Score
1	JACC-Cardiovascular Imaging	8,801	10.975	0.026160
2	MEDICAL IMAGE ANALYSIS	7,694	8.880	0.013370
3	IEEE TRANSACTIONS ON MEDICAL IMAGING	19,545	7.816	0.024990
4	RADIOLOGY	54,641	7.608	0.061300
5	JOURNAL OF NUCLEAR MEDICINE	27,551	7.354	0.037990
6	EUROPEAN JOURNAL OF NUCLEAR MEDICINE AND MOLECULAR IMAGING	15,406	7.182	0.024760
7	CLINICAL NUCLEAR MEDICINE	4,922	6.498	0.007680
8	INTERNATIONAL JOURNAL OF RADIATION ONCOLOGY BIOLOGY PHYSICS	45,833	6.203	0.046810
9	INVESTIGATIVE RADIOLOGY	6,563	6.091	0.011150
10	Circulation-Cardiovascular Imaging	5,456	5.813	0.018480
11	NEUROIMAGE	99,720	5.812	0.132720
12	ULTRASOUND IN OBSTETRICS & GYNECOLOGY	12,336	5.595	0.020140
13	European Heart Journal-Cardiovascular Imaging	5,498	5.260	0.021650
14	RADIOTHERAPY AND ONCOLOGY	17,873	5.252	0.027470
15	Photoacoustics	512	5.250	0.001330
16	JOURNAL OF CARDIOVASCULAR MAGNETIC RESONANCE	5,113	5.070	0.014020
17	ULTRASCHALL IN DER MEDIZIN	2,238	4.613	0.003700
18	HUMAN BRAIN MAPPING	22,040	4.554	0.043230
19	JOURNAL OF NUCLEAR CARDIOLOGY	3,711	4.112	0.004480
20	EUROPEAN RADIOLOGY	19,597	3.962	0.033870

Rank	Full Journal Title	Total Cites	Journal Impact Factor	Eigenfactor Score
21	RADIOGRAPHICS	11,768	3.923	0.009170
22	Biomedical Optics Express	9,547	3.910	0.021750
23	MAGNETIC RESONANCE IN MEDICINE	32,648	3.858	0.034990
24	SEMINARS IN NUCLEAR MEDICINE	2,245	3.798	0.002710
25	Journal of the American College of Radiology	4,191	3.785	0.009760
26	JOURNAL OF MAGNETIC RESONANCE IMAGING	17,147	3.732	0.027800
27	KOREAN JOURNAL OF RADIOLOGY	2,687	3.730	0.004800
28	INTERNATIONAL JOURNAL OF HYPERTHERMIA	3,552	3.589	0.004020
29	EJNMMI Physics	394	3.475	0.001350
30	NMR IN BIOMEDICINE	7,511	3.414	0.014790
31	MOLECULAR IMAGING AND BIOLOGY	2,543	3.341	0.005360
32	Journal of Cardiovascular Computed Tomography	1,711	3.316	0.004430
33	COMPUTERIZED MEDICAL IMAGING AND GRAPHICS	2,464	3.298	0.002990
34	AMERICAN JOURNAL OF NEURORADIOLOGY	23,231	3.256	0.028010
35	MEDICAL PHYSICS	26,715	3.177	0.030870
36	AMERICAN JOURNAL OF ROENTGENOLOGY	33,633	3.161	0.028540
37	CANCER IMAGING	1,406	3.153	0.002220
38	Quantitative Imaging in Medicine and Surgery	1,072	3.074	0.002420
39	PHYSICS IN MEDICINE AND BIOLOGY	27,458	3.030	0.031970
40	EJNMMI Research	1,408	3.000	0.004320
41	EUROPEAN JOURNAL OF RADIOLOGY	12,871	2.948	0.019480
42	Radiation Oncology	5,669	2.895	0.012980

Selected JCR Year: 2018; Selected Categories: "RADIOLOGY, NUCLEAR MEDICINE and MEDICAL IMAGING"

Publications

D. Wenz, A. Kuehne, T. Huelnhagen, A.M. Nagel, H. Waiczies, O. Weinberger, C. Oezerdem, O. Stachs, S. Langner, E. Seeliger, B. Flemming, R. Hodge, T. Niendorf, “Millimeter Spatial Resolution In Vivo Sodium MRI of the Human Eye at 7 T Using a Dedicated Radiofrequency Transceiver Array”, *Magnetic Resonance in Medicine* 2018 Aug;80(2):672-684. https://doi.org/10.1002/mrm.27053.

D. Wenz, A.M. Nagel, J. Lott, A. Kuehne, S.C. Niesporek, T. Niendorf, „In Vivo Potassium MRI of the Human Heart at 7.0 Tesla“, *Magnetic Resonance in Medicine* 2019 Aug 27. https://doi.org/10.1002/mrm.27951. [Epub ahead of print].

Curriculum Vitae

Mein Lebenslauf wird aus datenschutzrechtlichen Gründen in der elektronischen Version meiner Arbeit nicht veröffentlicht.

List of publications

PEER REVIEWED PUBLICATIONS

[4] **D. Wenz**, A.M. Nagel, J. Lott, A. Kuehne, S.C. Niesporek, T. Niendorf, „In Vivo Potassium MRI of the Human Heart at 7.0 Tesla“, *Magnetic Resonance in Medicine* 2019 Aug 27. doi: 10.1002/mrm.27951. [Epub ahead of print]

[3] L. Boehmert, A. Kuehne, H. Waiczies, **D. Wenz**, T.E. Eigentler, S. Funk, F. von Knobelsdorff-Brenkenhoff, J. Schulz-Menger, A.M. Nagel, E. Seeliger, T. Niendorf, „Cardiorenal Sodium Magnetic Resonance Imaging using a Four/Four Channel ^{1}H/^{23}Na Radiofrequency Antenna Array“, *Magnetic Resonance in Medicine* 2019 Dec;82(6):2343-2356. doi: 10.1002/mrm.27880. Epub 2019 Jun 30.

[2] **D. Wenz**, A. Kuehne, T. Huelnhagen, A.M. Nagel, H. Waiczies, O. Weinberger, C. Oezerdem, O. Stachs, S. Langner, E. Seeliger, B. Flemming, R. Hodge, T. Niendorf, “Millimeter Spatial Resolution In Vivo Sodium MRI of the Human Eye at 7 T Using a Dedicated Radiofrequency Transceiver Array”, *Magnetic Resonance in Medicine* 2018 Aug;80(2):672-684. doi: 10.1002/mrm.27053.

[1] K. Paul, T. Huelnhagen, E. Oberacker, **D. Wenz**, A. Kuehne, H. Waiczies, S. Schmitter, O. Stachs, T. Niendorf, “Multiband Diffusion-Weighted MRI of the Eye and Orbit Free of Geometric Distortions Using a RARE-EPI Hybrid”, *NMR in Biomedicine*, 2018 Mar;31(3). doi: 10.1002/nbm.3872

PEER REVIEWED CONFERENCE ABSTRACTS AND PRESENTATIONS

[20] **D. Wenz**, A.M. Nagel, A. Kuehne, T. Niendorf, „In Vivo Potassium MRI of the Human Heart at 7.0 Tesla", *ISMRM 27th Annual Meeting*, Montréal, Canada, 11-16 May, 2019. (Poster)

[19] T.E. Eigentler, L. Boehmert, A. Kuehne, **D. Wenz**, E. Oberacker, L. Winter, T. Niendorf, „Compact Self-Grounded Bow-Tie Antenna Building Block for Cardiac MRI at 7.0 Tesla”, *ISMRM 27th Annual Meeting*, Montréal, Canada, 11-16 May, 2019. (Talk)

[18] L. Boehmert, A. Kuehne, H. Waiczies, **D. Wenz**, T.E. Eigentler, A.M. Nagel, T. Niendorf „Cardiorenal Sodium MRI using an Eight Channel ^{1}H/^{23}Na Radiofrequency Antenna Array”, *ISMRM 27th Annual Meeting*, Montréal, Canada, 11-16 May, 2019. (Pitch)

[17] L. Boehmert, A. Kuehne, H. Waiczies, **D. Wenz**, T.E. Eigentler, A.M. Nagel, T. Niendorf „Cardiorenal Sodium MRI using an Eight Channel ^{1}H/^{23}Na Radiofrequency Antenna Array”, *ISMRM 27th Annual Meeting*, Montréal, Canada, 11-16 May, 2019. (Poster)

[16] **D. Wenz**, A.M. Nagel, A. Kuehne, T. Niendorf, „In Vivo Potassium MRI of the Human Heart at 7.0 Tesla", *ISMRM Workshop on Ultrahigh Field Magnetic Resonance: Technological Advances, Translational Research Promises and Clinical Applications*, Dubrovnik, Croatia, 29-31 March 2019. (Talk)

[15] T.E. Eigentler, L. Boehmert, A. Kuehne, **D. Wenz**, E. Oberacker, L. Winter, T. Niendorf, „Compact Self-Grounded Bow-Tie Antenna Building Block for Cardiac MRI at 7.0 Tesla", *ISMRM Workshop on Ultrahigh Field Magnetic Resonance: Technological Advances, Translational Research Promises and Clinical Applications*, Dubrovnik, Croatia, 29-31 March 2019. (Talk)

[14] L. Boehmert, A. Kuehne, H. Waiczies, **D. Wenz**, T.E. Eigentler, A.M. Nagel, T. Niendorf „Cardiorenal Sodium MRI using an Eight Channel $^{1}H/^{23}Na$ Radiofrequency Antenna Array", *ISMRM Workshop on Ultrahigh Field Magnetic Resonance: Technological Advances, Translational Research Promises and Clinical Applications*, Dubrovnik, Croatia, 29-31 March 2019. (Poster)

[13] **D. Wenz**, A. Kuehne, T. Huelnhagen, A.M. Nagel, H. Waiczies, O. Stachs, E. Seeliger, B. Flemming, T. Niendorf, "High Definition Sodium (23Na) In Vivo MRI of the Human Eye at 7.0 Tesla: Need for Substantially Enhanced Spatial Resolution than Commonly Used in Brain MRI", *ISMRM-ESMRMB Joint Meeting*, Paris, France, 16-21 June 2018. (Poster)

[12] **D. Wenz**, N.G.R. Behl, A.M. Nagel, M.E. Ladd, T. Niendorf, "Application of 3D-Dictionary Learning Compressed Sensing Reconstruction En Route to Isotropic Submillimeter Spatial Resolution Sodium (23Na) In Vivo MRI of the Human Eye at 7.0 Tesla", *ISMRM-ESMRMB Joint Meeting*, Paris, France, 16-21 June 2018. (Poster)

[11] **D. Wenz**, A. Kuehne, T. Huelnhagen, A.M. Nagel, H. Waiczies, O. Stachs, E. Seeliger, B. Flemming, T. Niendorf, "Sodium (23Na) In Vivo Magnetic Resonance Imaging of the Human Eye at 7.0 Tesla: a New Tool to Investigate Ocular Disorders", *Association for Research in Vision and Ophthalmology Annual Meeting*, Hawaii, USA, 2018. (Poster)

[10] **D. Wenz**, A. Kuehne, T. Huelnhagen, A.M. Nagel, H. Waiczies, O. Stachs, E. Seeliger, B. Flemming, T. Niendorf, "High Definition Sodium (23Na) In Vivo MRI of the Human Eye at 7.0 Tesla: Need for Substantially Enhanced Spatial Resolution than Commonly Used in Brain MRI", *ISMRM Workshop on MR Imaging of nX-Nuclei (23Na & Friends): From Controversies to Potential Clinical Applications*, Dubrovnik, Croatia, 7-10 April, 2018. (Poster)

[9] **D. Wenz**, N.G.R. Behl, A.M. Nagel, M.E. Ladd, T. Niendorf , "Application of 3D-Dictionary Learning Compressed Sensing Reconstruction En Route to Isotropic Submillimeter Spatial Resolution Sodium (23Na) In Vivo MRI of the Human Eye at 7.0 Tesla", *ISMRM Workshop on MR Imaging of nX-Nuclei (23Na & Friends): From Controversies to Potential Clinical Applications*, Dubrovnik, Croatia, 7-10 April, 2018. (Poster)

[8] **D. Wenz**, A.M. Nagel, N.G.R. Behl, A.W. Magill, R. Umathum, A. Kuehne, T. Niendorf, "Potassium (39K) In Vivo MRI of the Human Heart at 7.0 Tesla: Feasibility Study", *ISMRM Workshop on MR Imaging of nX-Nuclei (23Na & Friends): From Controversies to Potential Clinical Applications*, Dubrovnik, Croatia, 7-10 April, 2018. (Poster)

[7] L. Boehmert, H. Waiczies, C. Oezerdem, **D. Wenz**, A. Kuehne, A. Pohlmann, T. Niendorf, „Quadrature Birdcage RF Coil for Sodium (23Na) Imaging in Rodents at 9.4 T: Initial Results", *8th Annual Scientific Symposium on Ultrahigh Field Magnetic Resonance*, Berlin, Germany, 30th June, 2017. (Poster)

[6] **D. Wenz**, A. Kuehne, T. Huelnhagen, A.M. Nagel, H. Waiczies, O. Weinberger, C. Oezerdem, O. Stachs, S. Langner, E. Seeliger, B. Flemming, R. Hodge, T. Niendorf, „Millimeter Spatial Resolution In Vivo Sodium MRI of the Human Eye at 7.0 Tesla Using a Dedicated Radiofrequency Transceiver Array", *8th Annual Scientific*

Symposium on Ultrahigh Field Magnetic Resonance, Berlin, Germany, 30th June, 2017. (Poster)

[5] C. Oezerdem, T. Huelnhagen, A. Kuehne, **D. Wenz**, J. Millward, L. Winter, T. Niendorf, "Lighter is better: A Flexible Lightweight Eight Channel Slot Antenna Array for Cardiac MRI at 7.0 Tesla", *ISMRM 25th Annual Meeting*, Hawaii, USA, 22-27 April, 2017. (Talk)

[4] **D.Wenz**, O. Weinberger, A. Kuehne, H. Waiczies, A.M. Nagel, C. Oezerdem, T. Huelnhagen, D. Lysiak, L. Winter, O. Stachs, S. Langner, E. Seeliger, B. Flemming, T. Niendorf, "Panning for Salt: One Millimeter Resolution In Vivo Sodium MRI of the Human Eye at 7.0 Tesla Using a Six Channel Transceiver Array", *ISMRM 25th Annual Meeting*, Hawaii, USA, 22-27 April, 2017. (Talk)

[3] **D. Wenz**, C. Oezerdem, O. Stangl, T. Huelnhagen, E. Oberacker, T. Niendorf, "Towards High-Fidelity Sodium MRI of the Human Eye at 7.0 T: Preliminary Results with a Six Channel Transceiver Array", *7th Annual Scientific Symposium on Ultrahigh Field Magnetic Resonance*, Berlin, Germany, 24th June, 2016. (Poster)

[2] **D. Wenz**, C. Oezerdem, O. Stangl, T. Huelnhagen, E. Oberacker, T. Niendorf, "High-Fidelity Sodium MRI of the Human Eye at 7.0 T: Preliminary Results with a Six Channel Transceiver Array", *ISMRM Workshop on Ultra High Field MRI: Technological Advances & Clinical Applications*, Heidelberg, Germany, 6-9 March, 2016. (Poster)

[1] **D. Wenz**, O. Stangl, C. Oezerdem, L. Winter, T. Niendorf, "Gandhi Coil Design: First Step Towards Further Development of RF Coils Tailored for Na-23 Human Eye Imaging at 7T.", *6th Annual Scientific Symposium on Ultrahigh Field Magnetic Resonance*, Berlin, Germany, 26th June, 2015. (Poster)

Acknowledgements

First of all, I would like to thank Prof. Thoralf Niendorf for giving me this great opportunity to work in his group. Thank you for supervising my work and motivating me to always push the boundaries. This was a great adventure, full of eye-opening lessons which helped me to develop as a young scientist. I will keep pushing!

Many thanks to all of my friends from Berlin Ultrahigh Facility at Max Delbrück Center for Molecular Medicine. Thank you for making our daily life happier. I hope we will meet soon!

I would like to use this opportunity to acknowledge my dear collaborators: people from MRI.TOOLS, especially André Kühne and Darius Lysiak; Russel Hodge (MDC), Armin Nagel (University of Erlangen), Oliver Stachs (University of Rostock), Nicolas Behl (DKFZ Heidelberg; currently Siemens Healthineers) for our fruitful collaboration.

Dedykuję tę pracę moim najbliższym, którzy dali mi tak dużo miłości i nigdy nie pozwolili mi w siebie zwątpić.